INAF
ISTITUTO NAZIONALE
DI ASTROFISICA
NATIONAL INSTITUTE
FOR ASTROPHYSICS

Publication Year	2020
Acceptance in OA	2025-03-14T14:54:49Z
Title	X-ray computed tomography: Morphological and porosity characterization of giant Antarctic micrometeorites
Authors	Dionnet, Zelia, Suttle, Martin D., LONGOBARDO, Andrea, Rotundi, Alessandra, Folco, Luigi, DELLA CORTE, Vincenzo, King, Andrew
Publisher's version (DOI)	10.1111/maps.13533
Handle	http://hdl.handle.net/20.500.12386/36811
Journal	METEORITICS & PLANETARY SCIENCE
Volume	55

Check for updates

The Meteoritical Society

Meteoritics & Planetary Science 55, Nr 7, 1581–1599 (2020)
doi: 10.1111/maps.13533

X-ray computed tomography: Morphological and porosity characterization of giant Antarctic micrometeorites

Zelia DIONNET *[1,2], Martin D. SUTTLE [3,4], Andrea LONGOBARDO[1,2], Alessandra ROTUNDI[1,2], Luigi FOLCO [3,5], Vincenzo DELLA CORTE[2], and Andrew KING[6]

[1]Università di Napoli "Parthenope," DIST, Centro Direzionale Isola C4, I-80143 Naples, Italy
[2]INAF-IAPS, via Fosso del Cavaliere 100, I-00133 Rome, Italy
[3]Dipartimento di Scienze della Terra, Università di Pisa, V. S. Maria 53, I-56126 Pisa, Italy
[4]Planetary Materials Group, Department of Earth Science, The Natural History Museum, Cromwell Rd, London SW7 5BD, UK
[5]CISUP, Centro per l'Integrazione della Strumentazione dell'Universita di Pisa, Pisa, Italy
[6]PSICHE Beamline, Synchrotron SOLEIL, Gif-Sur-Yvette, France
*Corresponding author. E-mail: zelia.dionnet@uniparthenope.it

(Received 21 November 2019; Revised 08, April 2020; revision accepted 19 May 2020)

Abstract–Giant micrometeorites (MMs; 400–2000 μm) are exceedingly rare and scientifically valuable. Three-dimensional nondestructive characterization by X-ray computed tomography (X-CT) provides information on the petrography and thus petrogenesis of MMs and serves as a guide to maximize subsequent multi-analytical studies on such precious planetary materials. Here, we discuss the results obtained by X-CT on 22 giant MMs and the classification based on their 3-D density contrast images. Scoriaceous and unmelted MMs have distinct porosity ranges (10–40 vol% versus 0–25 vol%, respectively). We observe a porosity variation inside scoriaceous MMs, which allows their atmospheric entry flight history to be resolved. For the first time, spinning entry is explicitly demonstrated for four partially melted MMs. Furthermore, we are able to resolve the thermal gradient in a single particle, based on porosity variation (seen as a progressive increase in pore abundance and size with higher peak temperatures). Moreover, we explore parent body alteration through the 3-D analysis of pores distribution, showing that shock fabrics are either absent or weakly developed in our data set. Finally, owing to the detection of pseudomorphic chondrules, we estimate that the intensively aqueously altered C1 or CI-like material could represent 18% of the MM flux at this size fraction (400–1000 μm).

INTRODUCTION

Micrometeorites (MMs) are extraterrestrial dust grains, <2 mm in diameter, derived from asteroids and comets (Genge et al. 2008). The microanalysis of these valuable samples allows us to better understand the primitive bodies of the solar system and the processes undergone before and/or after accretion. In particular, the compositional heterogeneity of primitive bodies is the result of a complex set of pre- and post accretionary processes related to the evolution of the early solar system and to the planet-forming age (Alexander et al. 2007). MMs are derived from a larger variety of the small bodies as compared to macroscopic meteorites due to different delivery mechanism (Vokrouhlický et al. 2008; Genge et al. 2008). Furthermore, giant MMs (>400 μm) are more representative of their parent body lithology and thus can contain coarse-grained components such as chondrules and calcium-aluminum inclusions (CAIs). However, because giant MMs are especially rare (Taylor et al. 2007), it is critical to optimize the sample analysis sequence. In addition, in light of new sample return missions, that is, Hayabusa2/JAXA (Kitazato et al. 2019; Sugita et al. 2019; Watanabe et al. 2019), OSIRIS-Rex/NASA (Lauretta et al. 2015), and MMX/JAXA (Campagnola et al. 2018), defining the most efficient sequence of analytical techniques to maximize the results obtainable on small

© The Meteoritical Society, 2020.

and rare extraterrestrial materials represents a critical issue (Nakamura et al. 2014). Three-dimensional non-destructive analysis plays a crucial role in such a sequence. As an example, X-ray computed tomography (X-CT) was one of the first techniques applied to the analysis of the Itokawa particles (Nakamura et al. 2011; Tsuchiyama et al. 2011). In addition, it was used to characterize cometary particles brought to Earth by the STARDUST space probe (Nakamura et al. 2008; Tsuchiyama et al. 2009).

X-CT is also a powerful stand-alone technique, that is, not necessarily as part of an analysis sequence, and is increasingly employed for the characterization of valuable samples (see Hanna and Ketcham [2018] for a review). Hanna and Ketcham (2018) discussed the distributions and the shape of chondrules inside primitive CM chondrites. Based on the detection of irregularly shaped chondrules, they proposed that "chondrules with a high degree of surface roughness accreted a relatively larger amount of nebular dust compared to smoother chondrules." Ebel and Rivers (2007) studied the porosity inside different classes of meteorites and have shown that regions of interest, such as CAI and chondrules, can be studied in detail while avoiding invasive sampling.

Several studies have analyzed giant MMs (Van Ginneken et al. 2012; Baecker et al. 2018; Cordier et al. 2018; Suttle et al. 2019a, 2019b), but very few include a 3-D sample characterization (e.g., Kohout et al. 2014). Kohout et al. (2014) studied the effect of atmospheric entry on MMs' porosity. They observed a rise of the porosity with increasing degree of atmospheric entry heating. However, distinguishing primary porosity originating from the sample's parent body history from secondary porosity formed during atmospheric entry remains challenging. Studying primary porosity is critical to understanding accretional and collisional processes in the early solar system (Consolmagno et al. 2008; Blum et al. 2017) as well as the activity of small bodies (Fulle et al. 2019). Taylor et al. (2011) studied the distribution and the shape of pores and metal beads inside 109 MMs. They concluded that the thermal decomposition of sulfide phases plays a critical role in the formation of secondary porosity and thus scoriaceous textures. The accurate characterization of the porosity and more importantly the distribution of vesicles are crucial for many processes such as impact-related (re)heating and microcracks, and thermal diffusion in asteroids (Flynn et al. 2018).

In the present work, we illustrate the potential of the X-CT characterization on a set of 22 unmelted and scoriaceous giant MMs with a size between 400 and 1000 μm (see Table 1). We explore how atmospheric entry and secondary processes can affect a set of MM characteristics: global porosity, its spatial variation inside the sample, shape and size distribution of the pores, the presence of rims, the distribution of the metallic components, and the presence of chondrules.

MATERIALS AND METHODS

We analyzed 22 giant MMs with sizes between 29×10^6 μm^3 and 116×10^6 μm^3 (see Table 1). They were collected by the PNRA (Programma Nazionale di Ricerca in Antartide) from an MM trap on the top of Miller Butte in the Transantarctic Mountains (Folco et al. 2008; Rochette et al. 2008; Suttle and Folco 2020). The processes of alteration experienced during their up to 1–2 million years long stay on Earth have been studied by Suavet et al. (2009, 2011) and Van Ginneken et al. (2016). We first classified the samples into scoriaceous and unmelted types, following the classification of Genge et al. (2008), by means of scanning electron microscope (SEM) observations on their external surfaces (carried out without coating in low-vacuum mode using an FEI ESEM-FEG QUANTA 450 at the Centro per l'Integrazione della Strumentazione dell'Università di Pisa, CISUP, Italy). This classification is based on the degree of thermal reprocessing during atmospheric entry and on the terrestrial alteration undergone by MMs. We can see small traces of weathering for some of the samples (as in TAM 50.08, TAM 50.11, TAM 50.15, and TAM 50.29), in which we observe thin weathering external rims on particle exteriors. Because weathering can alter the primary porosity and even vesicles (Van Ginneken et al. 2016), for our study, we selected 22 MMs with a low degree of terrestrial weathering. Thus, terrestrial weathering should affect only the surface of a few MMs in our collection and be negligible for the inside of our samples.

Characterization in 3-D was performed at the synchrotron X-ray beamline PSICHE at SOLEIL synchrotron (France). We measured 1200 2-D projections of the linear attenuation coefficient (LAC) at regular rotation intervals of 0.15° in order to reconstruct the variations of the LAC in 3-D. X-CT was performed with a parallel monochromatic beam of 25.5 keV and with an exposure time of 250 ms per projection. The final voxel size is ~0.6 μm. With this technique, we are therefore able to characterize porosity and the presence of structures inside the samples without destroying them. By utilizing high-intensity, monochromatic synchrotron radiation, we were able to rapidly (<25 min) scan each sample while maintaining high signal-to-noise and high image resolution. Post-processing 3-D reconstruction was achieved using the Python library Tomopy (Gürsoy et al. 2014).

19455100, 2020, 7, Downloaded from https://onlinelibrary.wiley.com/doi/10.1111/maps.13533 by CochraneItalia, Wiley Online Library on [27/02/2025]. See the Terms and Conditions (https://onlinelibrary.wiley.com/terms-and-conditions) on Wiley Online Library for rules of use; OA articles are governed by the applicable Creative Commons License

Table 1. List of the samples with their main characteristic: A is the anisotropic degree of the pores distribution and E its elongation index; the description of the chondrules and their size (ps = pseudomorphic); the parent bodies were inferred thanks to oxygen isotopic composition analyses (see Suttle et al. [2019a] and Suavet et al. [2010] for the description of Group 4 properties) and the petrographic types from the texture; the entry flight history is inferred from the variation of porosity.

Sample ID	Class	Subclass	Vol (10^6 μm^3)	Porosity (±3%)	*A* (±0.1)	*E* (±0.01)	Presence of chondrules	Diameter of chondrules (μm × μm)	Inferred petrographic types	Inferred entry flight history
TAM 50.01	Sc	Fine-grained	35	30	1.46	1.06	–	–	–	–
TAM 50.03	Sc	Fine-grained	49	27	2.63	1.13	–	–	–	Fragmented
TAM 50.09	Sc	Coarse-grained	46	18	6.45	1.43	Intact	460 × 670	2/4	–
TAM 50.10	Sc	Fine-grained	87	36	3.68	1.30	–	–	–	–
TAM 50.12	Sc	Coarse-grained	116	33	2.58	1.27	–	–	–	Spinning
TAM 50.15	Sc	Composite	82	22	2.49	1.18	Intact	170 × 160	2/4	Spinning
TAM 50.17	Sc	Fine-grained	70	33	2.47	1.37	–	–	–	–
TAM 50.20	Sc	Composite	64	38	3.15	1.31	–	–	–	Spinning
TAM 50.21	Sc	Fine-grained	49	28	2.24	1.12	–	–	–	Spinning
TAM 50.22	Sc	Composite	76	12	1.26	1.08	Intact	280 × 480	2/4	–
TAM 55.01	Sc	Fine-grained	29	26	1.47	1.07	ps	200 × 150	1/2	–
TAM 60.03	Sc	Fine-grained	38	31	6.96	1.24	–	–	–	–
TAM 50.04	UM	Composite	28	23	1.80	1.11	Hydrated clast	80 × 80	C1	–
TAM 50.05	UM	Coarse-grained	92	8	2.83	1.25	–	–	–	–
TAM 50.07	UM	Fine-grained	39	10	1.57	1.14	–	–	–	–
TAM 50.08	UM	Coarse-grained	29	27	1.55	1.10	–	–	–	–
TAM 50.11	UM	Fine-grained	106	3	3.84	1.21	Intact	Several from 100 to 280	2/4	–
TAM 50.16	UM	Composite	72	12	2.31	1.17	–	–	–	–
TAM 50.25	UM	Fine-grained	80	23	2.91	1.28	ps	215 × 250	1/2	–
TAM 50.26	UM	Fine-grained	49	20	1.62	1.12	ps	–	1/2	–
TAM 50.29	UM	Coarse-grained	63	11	1.64	1.15	Intact	380 × 620	2/4	–
TAM 50.30	UM	Fine-grained	56	23	5.46	1.37	ps	125 × 125	1/2	–

The LAC is sensitive to the atomic number of the probed matter, meaning that features with high density contrast, such as pores or Fe-rich phases, can be easily resolved. As the first step of the analysis, we segmented our data using an LAC threshold following three components: pores, silicate phases, and Fe-rich areas

19455100, 2020, 7, Downloaded from https://onlinelibrary.wiley.com/doi/10.1111/maps.13533 by CochraneItalia, Wiley Online Library on [27/02/2025]. See the Terms and Conditions (https://onlinelibrary.wiley.com/terms-and-conditions) on Wiley Online Library for rules of use; OA articles are governed by the applicable Creative Commons License

(metal, sulfide, and metal-oxides). An example of the results of the segmentation is given in Fig. 1b for a slice inside TAM 50.15. We considered the voxels to be Fe-rich areas, when LAC >20. Voxels with LAC between 2 and 20 were assigned to silicate phases. After having defined the contour of the sample, we distinguished empty voxels, that is, having LAC <2, which correspond to pores inside the sample in 3-D. The LAC is not sensitive to low-Z materials (being Z the atomic number); thus, some of the empty voxels may contain low-Z material as organic matter. Matrajt et al. (2012) have observed different types of organic matter in extraterrestrial material using in situ transmission electron microscope. They observed organic globules with a size from 30 to 500 nm; thus, similar features may be contained inside the pore distribution observed in our samples and the smallest ones have sizes similar to the voxel in our study. Spongy organic materials can also have a size of a few nanometers and not be visible in our case, as the mixture with the mineral happens at a scale smaller than our pixel size. Even if we fail to detect the organic component with X-CT, in chondritic materials, it represents only a small percentage of the sample's mass (Standford et al. 2016). Moreover, using IR reflectance spectroscopy on reflection on the inside of one sectioned TAM MM, we have checked that the quantity of organic matter inside our sample is comparable to that measured in carbonaceous chondrites. Thus, the number of empty voxels, and the porosity, may be a slight overestimate, as up to 3% of the sample can be occupied by organic matter, but this source of uncertainty fits inside the one already given for the porosity (3%).

After data segmentation, we measured the porosity by counting the number of empty voxels inside the samples dividing by the number of voxels composing the sample. Specially written programs in Python were used for the segmentation of the images and the calculation of the porosity. Among the pores present inside our samples, we can distinguish diverse populations as (1) inter-granular (or accretional) pores, which are interpreted to be inter-grain pore spaces that were never destroyed by compression if and when the parent body experienced impact deformation (Scott and Krot 2003). These generally correspond to small pores present in the less-heated parts of our samples. (2) Cracks are also present either due to impact shock processing (Decarli et al. 2001; Suttle et al. 2017a) or formed by dehydration of phyllosilicates during atmospheric entry heating (Suttle et al. 2017b, 2019b). We classify pores as cracks when they present a clear elongated and branching shape. (3) Finally, during atmospheric entry, vesicles can be formed due to melting and degassing of volatile phases (Genge 2017b).

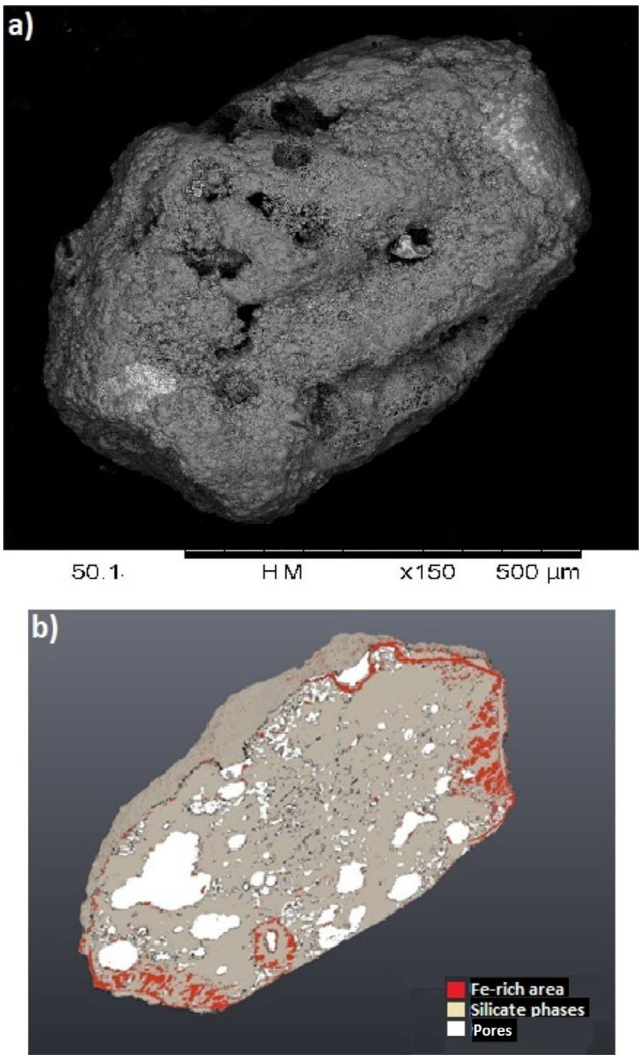

Fig. 1. a) SEM image of TAM 50.15. b) Segmentation of the same sample, visualization of Fe-rich areas (red), silicate phases (brown), and pores (white). (Color figure can be viewed at wileyonlinelibrary.com.)

We use the term vesicle only when we are confident that these pores have been formed during atmospheric entry and mainly to refer to round and well-defined pores in scoriaceous MMs.

The data also allowed the study of the size and the shape distributions of the voids with a resolution of 0.6 µm. We used the software Blob3D (Ketcham 2005) to estimate the size of each pore and generate a size distribution. The study of the shape of pores was performed using the software Quant3D (Ketcham 2005; Ketcham and Ryan 2004). We generated a random distribution of points inside the volume, and for every point inside a pore, we measured the distance, in 3-D, from the point to the pore edge. The contributions of all random distribution points are summed to obtain

19455100, 2020, 7, Downloaded from https://onlinelibrary.wiley.com/doi/10.1111/maps.13533 by CochraneItalia, Wiley Online Library on [27/02/2025]. See the Terms and Conditions (https://onlinelibrary.wiley.com/terms-and-conditions) on Wiley Online Library for rules of use; OA articles are governed by the applicable Creative Commons License

the total star volume distribution (SVD; see Ketcham 2005). A new 3-D space is generated to describe this distribution with its eigenvalues T_1, T_2, and T_3, which could be used to determine the strength of the SVD in each direction of the new space. (A visualization of the results of this procedure for two MMs will be shown in Fig. 5). To compare and describe our samples, we extracted two parameters: the anisotropic degree, A, that is, the ratio of the smaller to the higher eigenvalue:

$$A = T_1/T_3 \quad (1)$$

and E the elongation index:

$$E = 1 - T_2/T_1 \quad (2)$$

These two parameters give an estimation of the elongation of the pores compared to a spherical shape. These calculations provide a quantitative measure of petrofabric strength within the analyzed MMs.

We identified structures, such as chondrules, inside our samples, but their automated detection was prohibited because their LAC is not significantly different from that of the surrounding matrix. We thus detected and estimated their size manually.

RESULTS

The MMs that we analyzed here are both scoriaceous, with morphological properties affected by atmospheric entry, and unmelted. Following the classification of Genge et al. (2008): the studied population contains 12 fine-grained MMs; 5 coarse-grained MMs; and 5 composite MMs, which contain both fine-grained and coarse-grained parts. This classification gives an indication on the possible parent body for each sample. We present in Fig. 2 both SEM images and slices obtained by X-CT for four samples, illustrating classes and subclasses present in our set of samples. First, the variation in porosity is described according to the conventional MM classification system, and then, we will study the modification of morphology due to the atmospheric entry as seen in scoriaceous MMs and the ones due to secondary processes thanks to unmelted MMs.

Porosity

Global Porosity

We determined the porosity for each of the MMs studied (Fig. 3); this varies for the unmelted between 0 and 25 vol% and for the scoriaceous between 10 and 40 vol%. These values are consistent with the preliminary SEM analyses used to classify particles that noted large vesicles on the exterior of scoriaceous MMs. These gas cavities form during atmospheric entry (Genge 2017a).

In Fig. 3b, we examine how porosity varies between fine- and coarse-grained MMs. The fine-grained MMs have porosities between 9.2% and 35.9%. Similarly, the porosity of the coarse-grained particles varies between 7.6% and 32.5%. Thus, among our population, there is no clear relationship between sample porosity and pre-atmospheric texture. Interestingly however, TAM 50.12 has an anomalously high porosity value (32.5%). This is due to the presence of a single large vesicle in the center of the sample.

Variation of the Porosity Inside Single MMs

Variations in porosity were analyzed within single MMs in order to quantify the effect of heating.

TAM 50.03 has an unusual broadly pyramidal shape (see Figs. 4a and 4b). Two-dimensional tomographic slices through this particle show an asymmetric profile with a smooth concave edge (Fig. 4a) while the opposing edge has an irregular lobate form (Fig. 4a) In addition to the unusual shape, this MM exhibits systematic variations in porosity. This can be generally described by a progressive decrease in porosity away from the concave rounded edge (Fig. 4c). However, in detail, the profile is more complex. Entering the sample from the concave side, there is sudden increase in porosity, peaking at a value of ~29%, corresponding to the entry inside the sample at a given X (green arrow in Fig. 4a). Beyond this peak, a local minimum (around 22–24%) appears at depths of approximately 50 μm. Porosity rises again, reaching values around 30% before steadily decreasing linearly over the remaining ~350 μm (at a rate of approximately −1 vol% per 35 μm according to Y, without the fluctuations due to the voxel size) and dropping to a porosity minimum of 20% at the irregular lobate margin. During the early stages of atmospheric entry heating, MMs develop a thin melt layer, typically <100 μm thick that surrounds the particle's outer surface—this is termed an igneous rim (Genge 2006). Correlating porosity variation with the sample's texture demonstrates that the initial ~80 μm inside the sample (from the concave edge) corresponds to a thick igneous rim, while the remaining depth profile samples the MM's internal vesicular matrix.

Another interesting MMs is TAM 50.15, which has an elongated shape in the X direction (Fig. 5a) emphasized by an aspect ratio of 1.9:1 in the plane XY. We plotted the spatial distribution inside the MM of the high-density (Fe-rich) components and of the pores (see Fig. 5b). In this sample, Fe-Ni-S beads are primarily concentrated at either end of the particle, while the particle's core has a high porosity (20–30%,

19455100, 2020, 7, Downloaded from https://onlinelibrary.wiley.com/doi/10.1111/maps.13533 by CochraneItalia, Wiley Online Library on [27/02/2025]. See the Terms and Conditions (https://onlinelibrary.wiley.com/terms-and-conditions) on Wiley Online Library for rules of use; OA articles are governed by the applicable Creative Commons License

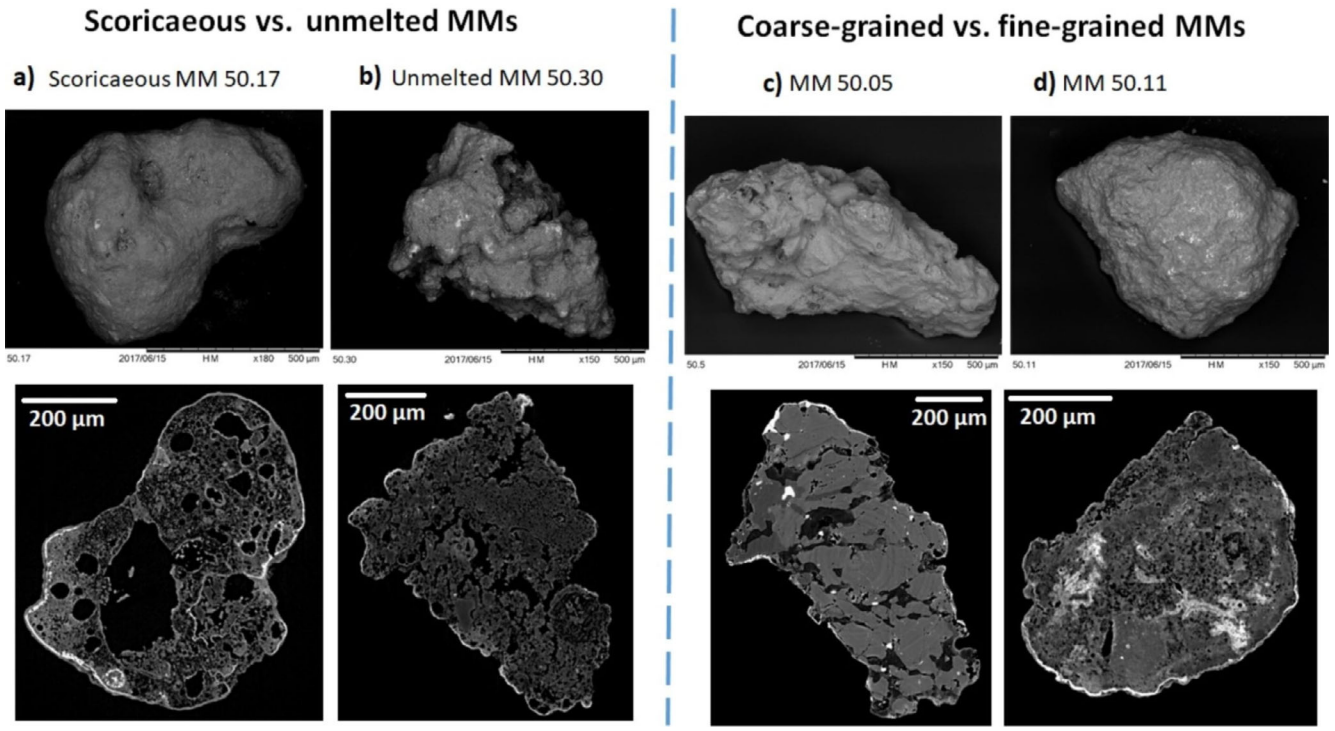

Fig. 2. Images of four MMs analyzed in this study. a) The scoriaceous MM 50.17, (b) the unmelted MM 50.30, (c) the MM 50.05 illustrate the case of coarse-grained MMs and (d) the MM 50.11 illustratea the case of fine-grained MMs. For each of them, we present an SEM images of the bulk specimen top) and a slide observed by X-CT (bottom). (Color figure can be viewed at wileyonlinelibrary.com.)

compared to the particle ends which have low porosities <20%). Thus, the locations of high- and low-density phases are anticorrelated.

In addition to TAM 50.15, two other MMs have similarly elongated shapes. These are TAM 50.20 (with an aspect ratio of 2.1:1) and TAM 50.21 (with an aspect ratio of 1.2:1). In both samples, porosity also rises toward the particle's center. In TAM 50.21, a high-density (Fe-rich) rim around the sample is observed.

Petrofabric

For each sample, we have estimated the anisotropic index of the cumulative distribution of voids. This reflects the aspect ratio of cavities. This metric varies from 1 to 6. A large anisotropy coefficient, like that calculated for TAM 50.30 (A = 5.46), indicates a strong petrofabric. Likewise, we also calculated E, the elongation index, measuring the degree of void elongation in a direction perpendicular to that of the anisotropy index. Regarding the distribution of A and E, there appears to be no significant difference between the unmelted and the scoriaceous populations. This is in contrast to the conclusions of Taylor et al. (2011) who observed elongated vesicles as common features in the case of scoriaceous MMs. The lack of correlation between the degree of melting (during atmospheric entry) and an MM's petrofabric suggests that these textural metrics are capable of measuring the sample's pre-atmospheric parent body structure.

Investigating whether individual MMs have a preferred orientation of their pore shapes provides an opportunity to explore the effects of impact-generated shock fabrics on the parent bodies of MMs. Although atmospheric entry processing may not alter a sample's parent body petrofabric, potentially subtle textural features will be progressively overprinted by degassing and melting effects. We therefore elected to investigate the shock histories of MMs only in those samples minimally affected by entry processing—that is in unmelted MMs. We have 10 unmelted MMs; their average anisotropy value is 2.46. Six of the samples have a value below this average (1.80, 1.57, 1.55, 2.31, 1.62, 1.64), three have slightly higher values between 2.83 and 3.84, and TAM 50.30 has a particularly large value (A = 5.46). Several scenarios could explain such high anisotropy index, such as multiples shocks in the history of the samples or important dehydration cracks. In Fig. 6, we show the star distribution value and an example of an X-CT slice for two samples, comparing a

19455100, 2020, 7, Downloaded from https://onlinelibrary.wiley.com/doi/10.1111/maps.13533 by CochraneItalia, Wiley Online Library on [27/02/2025]. See the Terms and Conditions (https://onlinelibrary.wiley.com/terms-and-conditions) on Wiley Online Library for rules of use; OA articles are governed by the applicable Creative Commons License

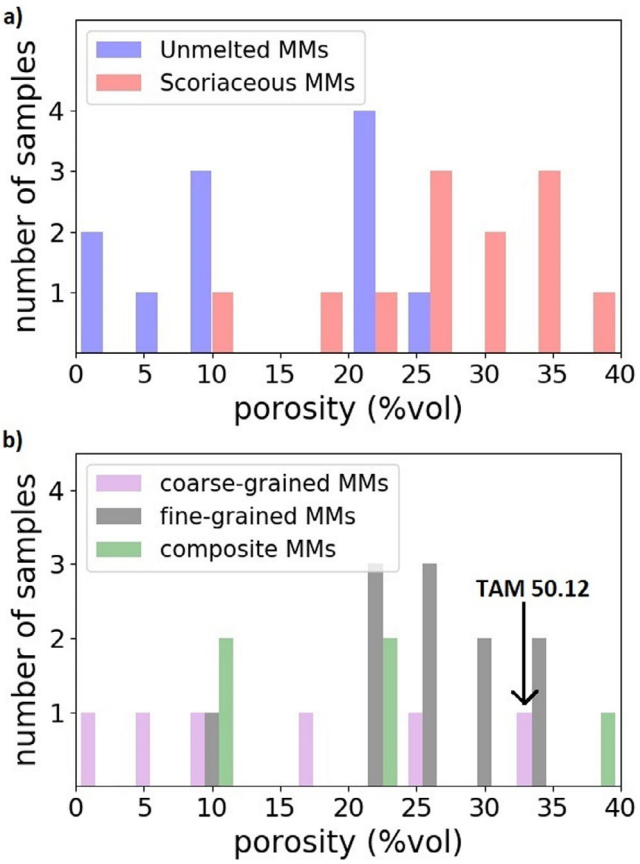

Fig. 3. a) MMs' porosity following the unmelted and scoriaceous classification; b) MMs' porosity according to coarse- and fine-grained classification. Binning of 4%. (Color figure can be viewed at wileyonlinelibrary.com.)

with a low anisotropy value (A = 1.8, TAM 50.04) with a higher one (A = 5.46, TAM 50.30).

Size Distribution of the Pores

We studied the vesicle size distributions inside the unmelted MMs to investigate how secondary processes can alter porosity developed during accretion. We plotted the distribution of the number of pores according to their volume. The cumulative number of pores is shown in Fig. 7 as we counted the number of pores bigger than a certain volume (given as x-axis).

Although the pore size distribution plots exhibit similar trends for the whole set of MMs, we found differences in their slope exponents, that is, the relative contribution of smaller pores with respect to the larger pores. This varies between −0.9 and −2.0. In Fig. 7, we present the results for three unmelted MMs. We calculated, using a line-of-best-fit, the slope of these distributions and then checked the correlation with the subclasses of each sample, that is, coarse-grained versus fine-grained and with their anisotropy coefficients. In their paper, Friedrich et al. (2008) studied the pore size distribution for a compacted ordinary chondrite and they concluded that the distribution of large pores (>2.8×10^{-5} mm) follows a power law with a coefficient of −0.75 between the log of the number of pores and the log of the volume of the subsequent pores. Finally, they had two hypotheses to explain such variation—it could be a peculiar property due to the compaction of this sample or the distribution observed could be typical of this class of meteorites. To compare with literature, a fit by a power law is also estimated for our data set. If we focus on big pores (> to 2.8×10^{-5} mm as Friedrich et al 2008), we obtain a coefficient of −0.96 for TAM 50.05, −1.32 for TAM 50.29, and −1.98 for TAM 50.30. The coefficients evaluated in our data are not comparable to the one measured on the macroscopic ordinary chondrite by Friedrich et al. (2008) and we did not find any conclusive correlation. It seems that pore size distribution and the sample's petrofabric are not clearly related.

Internal Solid Structures

In addition to porosity information, the tomographic data revealed the presence of coarse-grained inclusions within several of the MMs. These include TAM 50.04, TAM 50.09, TAM 50.15, TAM 50.11, and TAM 50.22 (shown in Fig. 8).

In TAM 50.04, one dark inclusion was identified. This has a low Z-contrast due to a low average atomic weight—this typically suggests an Mg-rich/Fe-poor composition. The inclusion has a rounded but non-spherical shape, an approximate size of 120 μm, and is porous with no discernible change in porosity between the inclusion and host matrix. Conversely, in TAM 50.09, almost the whole MM is coarse-grained, bearing only a thin discontinuous vesicular rim surrounding the particle's edge which has a brighter Z-contrast, indicating an Fe-enriched composition. This coarse-grained component contains rounded pores; Fe-rich metal droplets; and a series of dark, closely spaced linear features (possibly glassy mesostasis or melt veins between crystalline silicates). In TAM 50.15, the coarse-grained inclusion has the largest size, that is, around 200–250 μm, and is composed of darker material with abundant fractures. The boundary between the coarse-grained inclusion and the MM matrix is dull and therefore poorly defined. In TAM 50.11, multiple coarse-grained inclusions are present but also in this case, they are difficult to resolve from the MM's matrix due to similar Z-contrast. However, they have rounded spherical shapes and are commonly mantled by an Fe-rich phase—most likely metal or sulfide.

19455100, 2020, 7, Downloaded from https://onlinelibrary.wiley.com/doi/10.1111/maps.13533 by CochraneItalia, Wiley Online Library on [27/02/2025]. See the Terms and Conditions (https://onlinelibrary.wiley.com/terms-and-conditions) on Wiley Online Library for rules of use; OA articles are governed by the applicable Creative Commons License

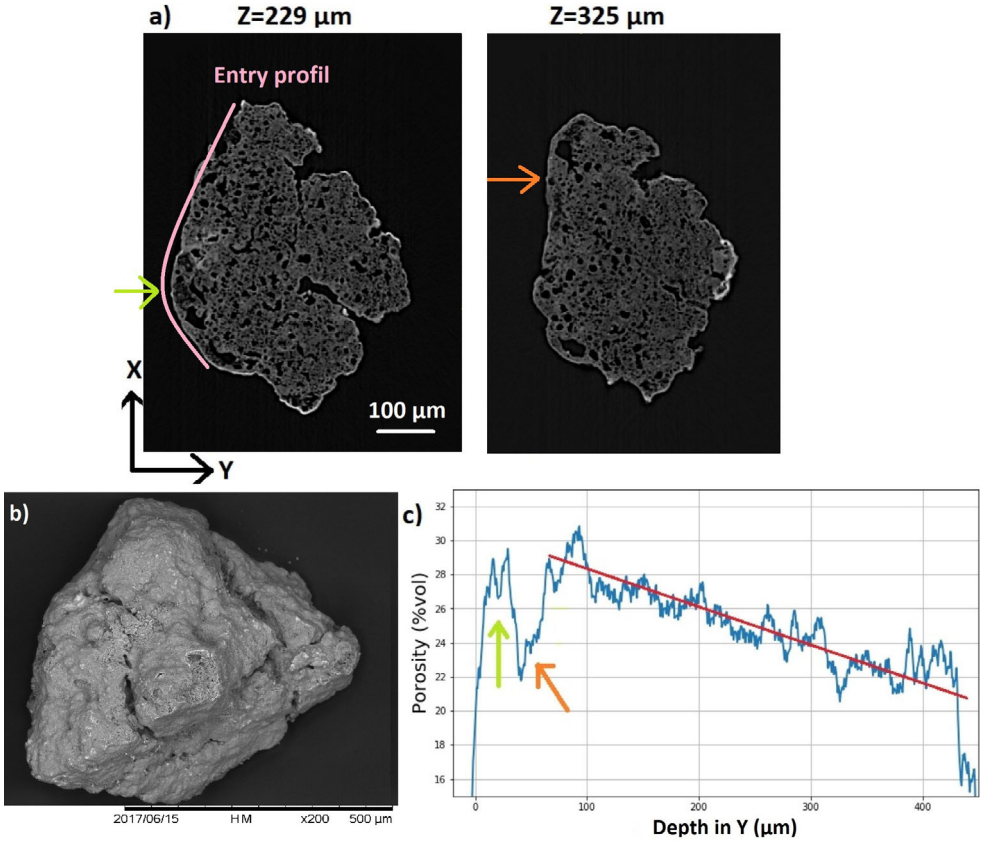

Fig. 4. a) Two slices in the XY plane of TAM 50.03 observed with X-CT. The MM front entrance into the Earth's atmosphere is shown in red. The shown slice is acquired at a height z = 229 microns from the bottom of the MM, corresponding to about the MM center. The green arrow represents the first non-empty slide, corresponding to the strong increase of porosity due to the sample in (c). On the second slice, the orange arrow shows "the second" entry in the sample in a perpendicular way. This slice is taken at 325 µm from the bottom of the sample. b) SEM pictures showing the external shape of the particles. c) Variation of the porosity among slices XZ when Y varies. (Color figure can be viewed at wileyonlinelibrary.com.)

Detection of Fe-rich components is also possible by using X-CT. Supporting MMs' classification, magnetic rims—described as "an external rim on the outer surface of igneous rims and usually surrounds the entire particle" by Genge (2006)—are easily detected, as for instance in TAM 50.17 (see Fig. 2), as well as Fe-Ni-S beads and their distribution (see TAM 50.09, TAM 50.15, and TAM 50.22 presented in Figs. 5 and 8).

DISCUSSION

The combined analysis of MMs' texture and porosity allows the investigation of their parent body alteration as well as of their atmospheric entry histories. Furthermore, the ability to characterize the sample non-destructively makes the X-CT a very efficient analytical technique for the preliminary analysis of rare materials such as the extraterrestrial ones. We will illustrate later how the X-CT can be used as part of a pre-characterization program for samples returned to Earth by space probes.

Porosity and Atmospheric Entry

Porosity: A Tool for Classification?

Among the giant TAM MMs analyzed here, the porosity varies between 0% and 40%: unmelted MMs have a porosity ranging between 0% and 25%, while for scoriaceous MMs, it ranges between 10% and 40%. These observations are consistent with previous studies, showing higher porosities inside the scoriaceous population as compared to the unmelted particles. Taylor et al. (2011) reported porosities between approximately 6% and 43% for scoriaceous MMs, while Kohout et al. (2014) observed average porosity for unmelted MMs between 0% and 12% and 16–25% for scoriaceous MMs. An explanation of this variation was given in Genge (2017a), who reported increasing vesicularity due to degassing of volatile-bearing phases during the atmospheric entry. Later, the porosity decreases as a result of migration of vesicles out of the particle.

19455100, 2020, 7, Downloaded from https://onlinelibrary.wiley.com/doi/10.1111/maps.13533 by CochraneItalia, Wiley Online Library on [27/02/2025]. See the Terms and Conditions (https://onlinelibrary.wiley.com/terms-and-conditions) on Wiley Online Library for rules of use; OA articles are governed by the applicable Creative Commons License

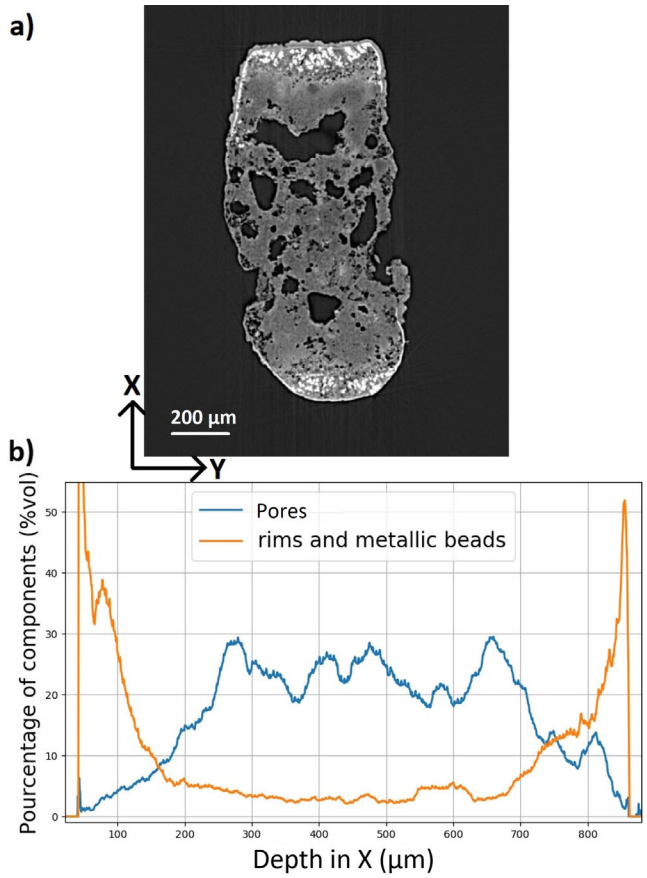

Fig. 5. a) X-CT images from the grain with the peculiar atmospheric entry: TAM 50.15. Notice the remarkable elongated shape according to the X direction. b) Variation of the concentration in heavy components (metallic beads and rims) and variation of the porosity among slices YZ (X varying). (Color figure can be viewed at wileyonlinelibrary.com.)

Experimental studies confirm that much of an MM's volatile budget is released prior to melting at subsolidus temperatures through the thermal decomposition of organics (<550 °C, Glavin and Bada 2001), phyllosilicates (300–800 °C, Che and Glotch 2012), and carbonates (~900 °C, Greshake et al. 1998; Court and Tan 2016). The majority of these gases can then escape through primary pore space (and newly generated dehydration cracks formed by phyllosilicate contraction) before the particle is sealed by an igneous rim (Taylor et al. 2011; Genge 2017a; Suttle et al. 2019b). However, once sealed newly generated volatile gases, mainly water vapor and gases derived from the decomposition of sulfides (Taylor et al. 2011) become trapped and lead to significant volume expansion and porosity increase (termed the parachute effect [Genge 2017a]). At this point, the particle may fracture explosively if internal gas pressures are not lowered by the formation of new escape channels (Suttle et al. 2019b). Longer duration heating or higher peak temperatures ultimately lead to the formation of cosmic spherules with a corresponding drop in porosity to below 10% (Taylor et al. 2011; Kohout et al. 2014).

We do not see any significant correlation between sample porosity and particle classification (as either fine- versus coarse-grained) (Fig 3b). Fine-grained MMs most likely derive from chondritic matrices (Genge et al. 2008a), and we therefore expect porosity between 10 and 35 vol%, as measured from carbonaceous chondrite (Consolmagno et al. 2008). This is the case for our 11 fine-grained specimens. In contrast, coarse-grained MMs are commonly found to be either chondrule material or samples of ordinary chondrites (Genge et al. 2008). Consolmagno et al. (2008) measured a porosity of around 10 vol% for ordinary chondrites. In our data, porosity of TAM 50.05 and TAM 50.29 is similar (7.6% and 10.5%) where it is higher for TAM 50.08, TAM 50.09, and TAM 50.12 (18%, 27%, and 33%, respectively). This difference may originate from the fact that our measurement was performed mainly on the matrix whereas Consolmagno et al. (2008) performed measurement on bulk (which contains chondrules with a lower porosity).

Submicron-sized voids (below the resolution of our analytical measurement capability) are likely to exist (Kohout et al. 2014), so the porosity measured in this work may be a bit underestimated. Helium pycnometry measurements can give access to the total sample porosity: several studies have compared results from this method and from X-CT to retrieve the porosity underestimation of the latter. Sasso et al. (2009) have shown that, even if 64% of the voids in ordinary chondrites are inter-granular, two-thirds of them can be detected by X-CT at a resolution of 8 µm per voxel. Friedrich et al. (2008) have also detected two-thirds of the voids on L chondrites at a similar resolution. More recently, Friedrich et al. (2017) have proven that with high resolution X-CT (2.6 µm per voxel), X-CT measurements are comparable to ideal gas pycnometry for ordinary chondrites. All our samples are not directly comparable to ordinary chondrites, but we used a very high spatial resolution (0.6 µm per voxel) compared to the previously mentioned studies, and thus, we estimate that we measure the majority (at the very least 66%) of the porosity.

Moreover, for the TAM 50.15, after embedding the sample within resin, the sample was sectioned for SEM examination. An estimation of the porosity was performed on this slice and compared with the same slice inside our 3-D volume reconstructed by X-CT. We did not find any significant difference between the two methods (<4% and thus comparable to the uncertainty

19455100, 2020, 7, Downloaded from https://onlinelibrary.wiley.com/doi/10.1111/maps.13533 by CochraneItalia, Wiley Online Library on [27/02/2025]. See the Terms and Conditions (https://onlinelibrary.wiley.com/terms-and-conditions) on Wiley Online Library for rules of use; OA articles are governed by the applicable Creative Commons License

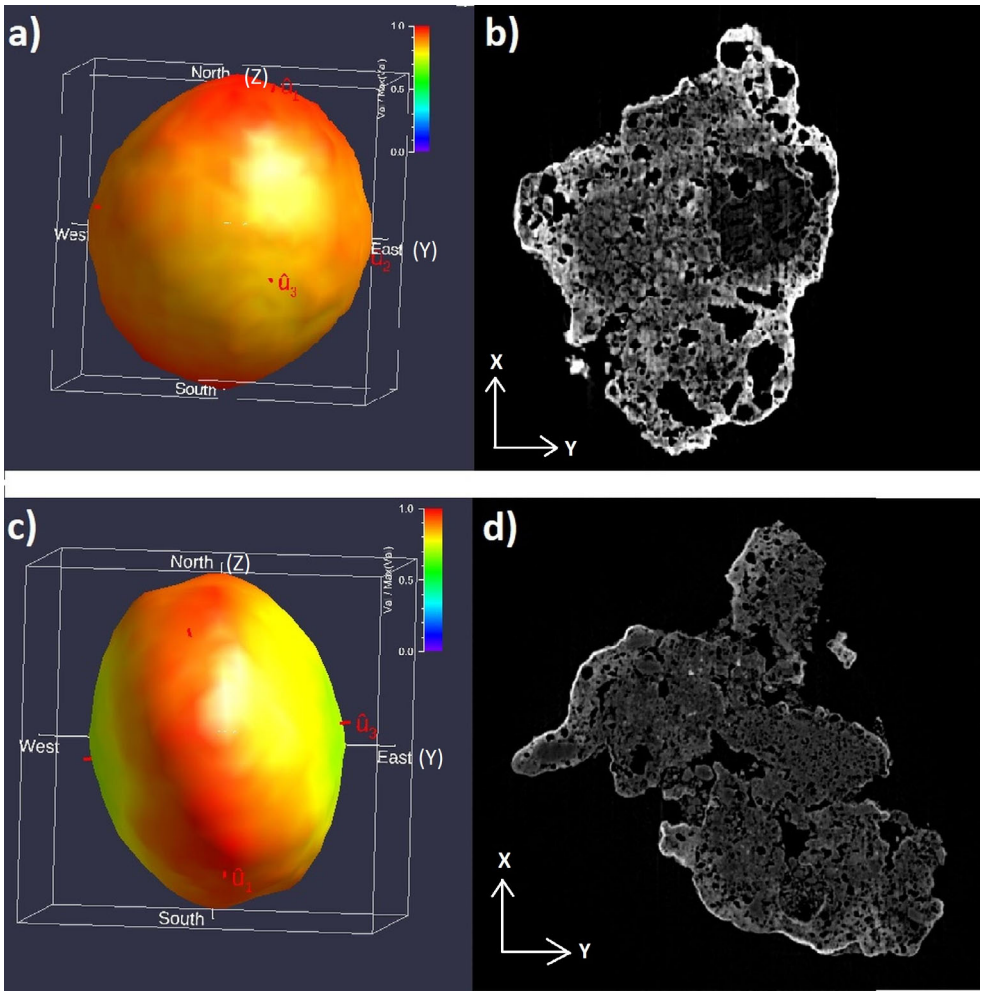

Fig. 6. X-CT porosity data from TAM MM 50.04 (a and b) and 50.30 (c and d). a, c) Cumulative distribution of pores. b, d) A X-CT slice of the vesicle specimen. (Color figure can be viewed at wileyonlinelibrary.com.)

given for our measurement with X-CT) and it confirms that the majority of the voids are detected with our X-CT setup.

Entry Flight History

Particle Fragmentation and Thermal Gradients

TAM 50.03 is a scoriaceous MM with highly unusual properties, both in terms of shape and internal texture. TAM 50.03 preserves an igneous rim with variable thickness around the specimen. On the curved concave side, the rim is well developed meanwhile on the opposite (irregular-shaped) side, the igneous rim is thin and poorly developed. These variations suggest a nonuniform heating of the MM during entry.

Previously, Suttle et al. (2019b) described the presence of giant TAM MMs with similar features; igneous rims of variable thickness and localized irregular-shaped regions on the exterior surfaces of otherwise smooth particles. They attributed these features to in-flight fragmentation occurring where volatile gases had become trapped within an MM's core. Trapped gases form a branching network of channels which receive enhanced heating of matrix adjacent to the channel walls. Where trapped gases form sufficient pressure to exceed the particle's tensile strength the MM fragments, resulting in the exposure of matrix material that was previously part of the particle's core. These newly exposed surfaces are then rapidly heated and new "secondary" igneous rims develop. However, because the duration of heating is necessarily shorter on the newly exposed surfaces, these secondary igneous rims are commonly thinner and less well developed. An asymmetric shape, variable thickness igneous rim, and smooth surface truncated by irregular-shaped regions are all features of TAM 50.03. Furthermore, on the irregular surface, in 2-D section (Fig. 4a), two prominent channels can be seen and these

19455100, 2020, 7, Downloaded from https://onlinelibrary.wiley.com/doi/10.1111/maps.13533 by CochraneItalia, Wiley Online Library on [27/02/2025]. See the Terms and Conditions (https://onlinelibrary.wiley.com/terms-and-conditions) on Wiley Online Library for rules of use; OA articles are governed by the applicable Creative Commons License

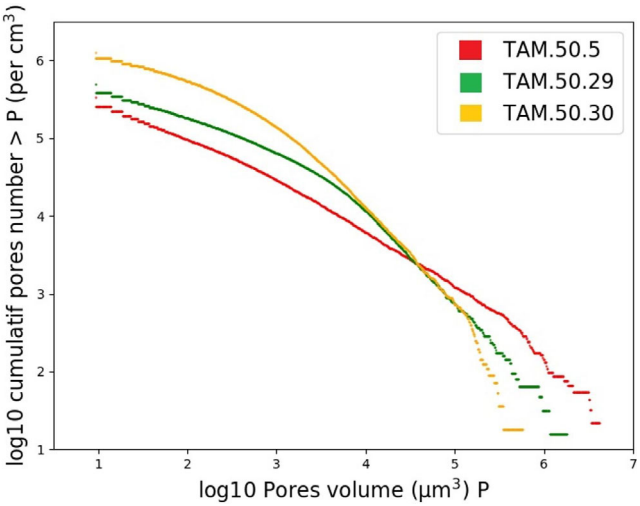

Fig. 7. Cumulative pores number bigger than P per cm^3 according to the pore volume P for TAM 50.05 (red), TAM 50.29 (green), and TAM 50.30 (orange). (Color figure can be viewed at wileyonlinelibrary.com.)

are nearly identical to those described in fig. 7 of Suttle et al. (2019b). Thus, the petrographic features of TAM 50.03 are consistent with an in-flight fragmentation event.

Previously, we noted that this MM also demonstrates a systematic trend of decreasing vesicle size across the particle's length, away from the curved, concave edge and toward the irregular-shaped edge (Fig. 4). If the concave edge represents the original external surface of the MM, while the irregular-shaped edge represents part of the MM's core that, after fragmentation, was exposed to a short period of heating, and thus reached a lower peak temperature, then we may expect a simple thermal gradient to exist within this MM fragment from the outer surface inward to the particle core.

In scoriaceous MMs, higher porosities are correlated with the degree of heating, and/or the peak temperature reached (Kohout et al. 2014; Genge 2017b). Thus, the observed linear trend of decreasing porosity across the particle away from the concave surface (29% to 21%) most likely represents the former thermal gradient that existed within the particle during atmospheric entry, with the highest temperatures and thus the highest porosity values at the outer surface (concave edge) and decreasing peak temperatures and decreasing porosity toward the center (represented by the irregular edge in TAM 50.03, due to its fragmented state).

By analyzing the sample's porosity variation, we can therefore explore the spatial variability in peak temperature within TAM 50.03. Scoriaceous MMs have experienced peak temperatures above the solidus and below the liquidus of hydrated chondritic material. Previous experimental work by Toppani et al. (2001) demonstrated that degree of melting is a function of heating duration, and thus, that kinetic effects act to limit the extent of melting in rapidly heated samples. Assuming typical entry conditions (flash heating <10s, Love and Brownlee 1991), vesicular and scoriaceous textures are generally reproduced between the range 1200 and 1600 °C (Toppani et al. 2001). Within TAM 50.03, the irregular edge (fragmented side) has the lowest porosity at about 22% and a distinctly vesicular texture. Thus, even the lowest temperature region of this MM experienced a moderate degree of melting (between 1200 and 1600°), combined with the thermal decomposition of volatiles, degassing, and vesicle formation, leading to expansion of the particle's volume in a "parachute effect" (Genge 2017a). Although previous studies have identified convincing evidence of high thermal gradients within MMs, for example, the existence of thermal fractured olivine (Genge et al. 2017), this is the first time that internal particle porosity, and by implication the spatial variation in thermal decomposition of volatiles, has been used to reconstruct thermal gradients within an MM, demonstrating a new application of µCT in planetary science.

Particles with Spinning Entry Histories

The morphology of some MMs preserves unique textural features inherited during their atmospheric entry. Previous studies on melted spherules have demonstrated that micrometeoroids can have both stable non-spinning flights as well as flights with high spin rates (Genge et al. [2016] and Genge 2017b). Evidence of stable flight histories includes cumulative settling of dense phases such as olivine and/or metal beads (Genge et al. 2016), the floating of low-density phases (i.e., vesicles) away from the particle's leading front (Genge et al. 2017), and the preservation of a coherent remnant magnetic field on cooling below the curie point (Suavet et al. 2011). Spinning cosmic spherules appear rarer but are evidenced by hollow spherules containing a single large off-center void (Suavet et al., 2011; Suttle and Folco 2020). Spinning dust is likely to be immature, that is, recently released from their parent asteroid, and because their rotation rates have not been yet dampened by magnetic effects (Genge 2017b), while particles with stable orientations are likely older dust, released a long time ago. Here, we identify both types of flight history on partially melted particles for the first time.

For MMs which enter the atmosphere with high rotation rates, centrifugal forces may act to deform

19455100, 2020, 7, Downloaded from https://onlinelibrary.wiley.com/doi/10.1111/maps.13533 by CochraneItalia, Wiley Online Library on [27/02/2025]. See the Terms and Conditions (https://onlinelibrary.wiley.com/terms-and-conditions) on Wiley Online Library for rules of use; OA articles are governed by the applicable Creative Commons License

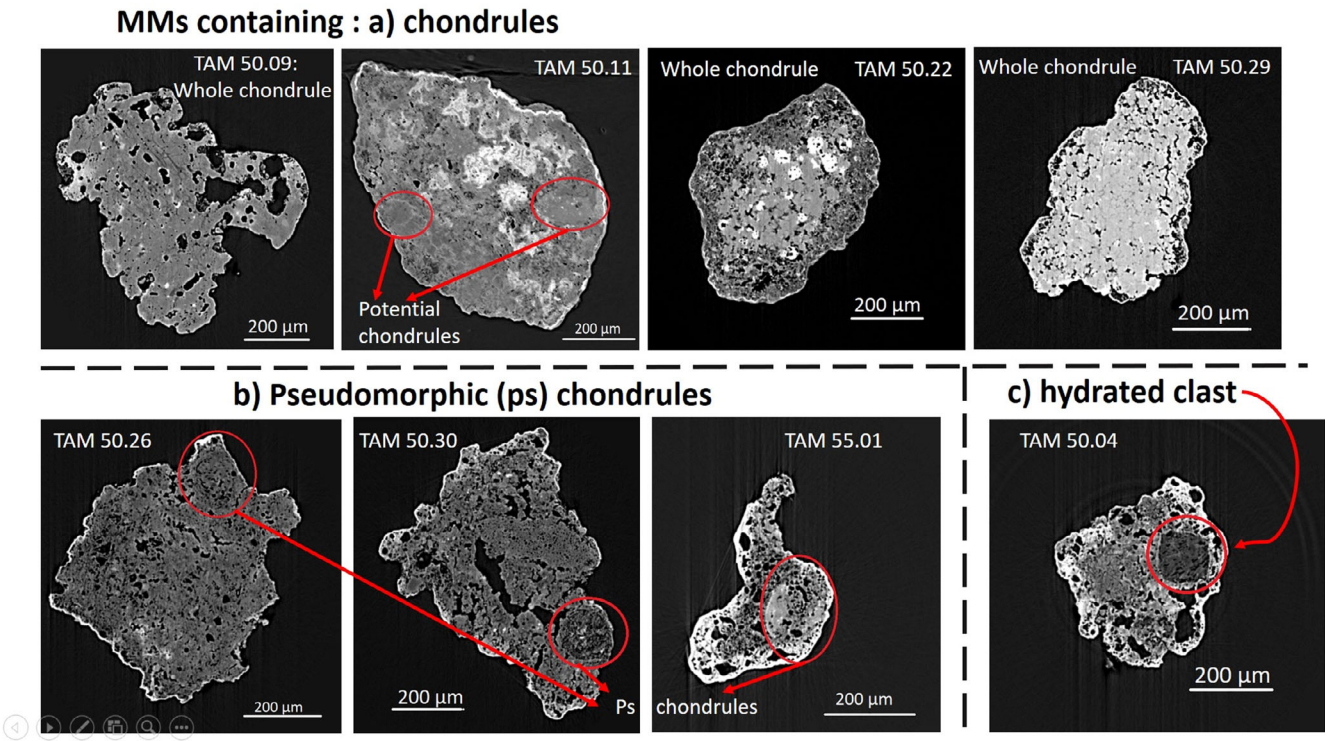

Fig. 8. SEM images showing features characteristics of (a) chondrules, (b) pseudomorphic chondrules, and (c) hydrated clast inside eight different TAM. (Color figure can be viewed at wileyonlinelibrary.com.)

their partially molten structures. Four of the particles studied here show evidence of spin-induced deformation. In the Porosity section, we described elongated MMs showing an apparent separation of phases (TAM 50.12, TAM 50.15, TAM 50.20, and TAM 50.21, see Fig. 9) based on phase density contrasts. Density separation occurs from the particle center outward. In TAM 50.15, TAM 50.20, and TAM 50.21, this has resulted in elongated and dumbbell-shaped particles (see Fig. 9). In TAM 50.15 (see Fig. 5), we observe a migration of the high-density phases toward the extremity of the sample and correspondingly, we note a progressive increasing of the porosity toward the particle's center. We observe large vesicles close to the lower half and the ends, and only small vesicles at the center. As similar description was given in Genge et al. (1997) for a dumbbell particle, this can be explained by a spinning entry with a spin perpendicular to the flight direction. Such a scenario, with a high rotation rate, was simulated by Genge (2017b) who modelled the migration of the vesicles toward the center of the MMs with very fast rotation (100–1000s radians per second). MMs with similar properties have also been described in the remnant magnetism study of Suavet et al. (2011) from metal bead-bearing cosmic spherules. Finally, the shape of the vesicle and distribution of components are consistent with a fast spinning entry and with a spin axis perpendicular to the flight direction. The low-density vesicles cannot, however, complete their migration to the particle's center and (presumed) spin axis because this is occupied instead by silicate inclusion, here interpreted as a partially melted chondrule (see the Chondrules, Pseudomorphs, Clasts, and Parent Body Alteration section).

In TAM 50.20, a similar high spin rate existed but instead the particle has a high-density coarse-grained rounded section and a lower density (melted) matrix, so the spin axis does not lay along the particle's volumetric axes. In TAM 50.12 (Fig. 9) which is transitional between a scoriaceous MM and a cosmic spherule, the particle has a single large off-center vesicle. This is a product of very high spin rates concentrating the lower density vesicles inward toward the particle's rotational axis. This process, described in Genge (2017b), is associated with immature dust.

Petrofabric Analysis

Parent body alteration processes on MMs have been studied with various analytical techniques, often requiring destructive analyses including resin-embedded polished sectioning. Here, we can give first indications for each particle without altering the 3-D structure.

19455100, 2020, 7, Downloaded from https://onlinelibrary.wiley.com/doi/10.1111/maps.13533 by CochraneItalia, Wiley Online Library on [27/02/2025]. See the Terms and Conditions (https://onlinelibrary.wiley.com/terms-and-conditions) on Wiley Online Library for rules of use; OA articles are governed by the applicable Creative Commons License

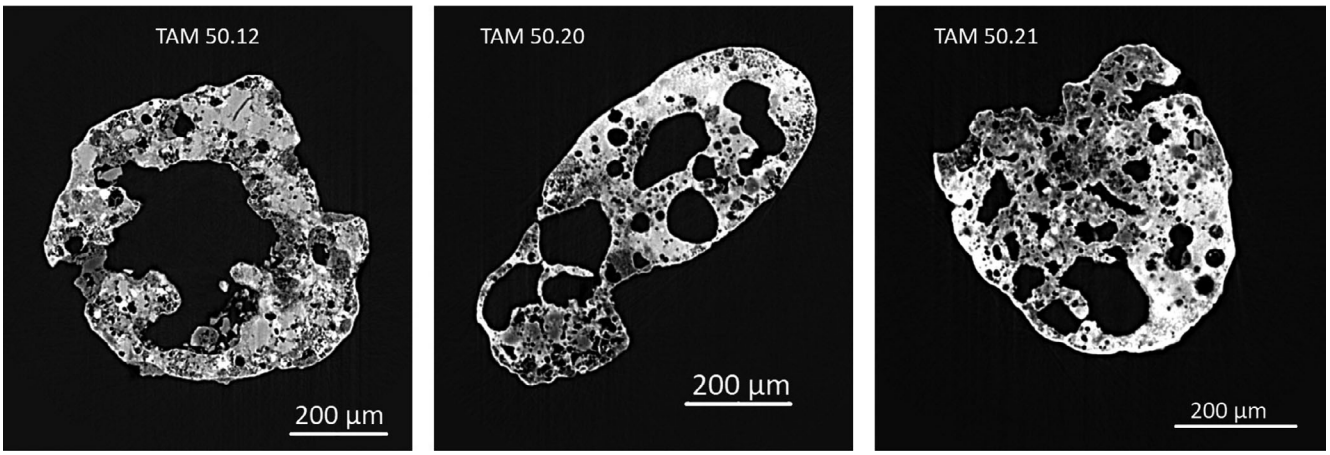

Fig. 9. SEM images of particles TAM 50.12, TAM 50.20, and TAM 50.21 with special atmospheric entry features.

The shape of the structures presents inside the MMs, especially the shape of the voids, provides important information: cracks testify either to shock processing on the parent bodies (De Carli et al. 2001; Suttle et al. 2017a) and/or thermal decomposition of phyllosilicate during atmospheric entry (Suttle et al. 2017b). Microcracks are produced by the passage of shock waves through a solid medium (DeCarli et al. 2001; Bowden 2002). The source of these shock waves could be impact cratering on the meteorite parent bodies. Friedrich and Rivers (2013) have shown that the structure of porosity has a regular relationship to the degree of compaction. In our samples, we noticed a preferred orientation shape of the voids with a privileged orientation. Samples with a higher anisotropy index have probably undergone higher intensity shocks or repeated shock events in a particular direction. Friedrich (2008), Hanna et al. (2015), and Benedix et al. (2008) have also studied the orientation of the different components in chondritic materials and they described privileged orientations of metals and voids, which they attributed to shock processing.

According to Woodcock and Naylor (1983), a sample is considered to have a strong petrofabric when $A > 50$, so our samples have undergone low to moderate shocks. Hanna et al. (2015) have estimated values comparable to ours (A between 1 and 3 for voids distribution inside the CM chondrite Murchison). Hanna et al. (2015) studied the distribution of metallic components in Murchison and showed that non-spherical shapes are the sign of a high degree of shock. A similar conclusion was found by Friedrich et al. (2008b). Since a significant fraction of the MM flux appears to be primarily derived from hydrated CM and CM-like bodies (Taylor et al. 2012; Suttle et al. 2017b), similarities in their petrofabric anisotropies further support a close genetic association.

A study of the porosity shape in unmelted MMs was also led by Taylor et al. (2011). They distinguished several types of MMs with predominantly round pores. However, they noticed that pores inside unmelted coarse-grained MMs are not round, but are defined by the shape of adjacent crystals. We have three coarse-grained unmelted MMs in our data set and the anisotropy index of the vesicle distribution are, respectively, 2.83 for TAM 50.05, 1.55 for TAM 50.08, and 1.64 for TAM 50.29. These values are not especially high and not similar to those found by Taylor et al. (2011).

We have tried to connect size distribution of pores with the parent's body class, but variation in the power law is not significantly different when comparing samples. Sasso et al. (2009) also measured the size distribution of pores in five samples from the same type (highly porous equilibrated ordinary chondrites) and they noticed differences similar to what we found. The pores size distribution is probably the most complicated parameter to interpret as it depends on the parent body's shock history, as well as on the degree of heating and the evaporation of the volatile phases during thermal metamorphism. Finally, this parameter may also be modified during atmospheric entry, at least in particles melted to some extent: with migration of vesicles due to the spin, larger vesicles can absorb the smaller one as they do not move at the same speed (Genge 2017b) thus affecting the vesicle size distribution. For the future, more statistics on this distribution in well-characterized samples will be very useful to isolate the contribution of each phenomenon.

Chondrules, Pseudomorphs, Clasts, and Parent Body Alteration

The most common components found within chondritic materials are chondrules—igneous assemblages

19455100, 2020, 7, Downloaded from https://onlinelibrary.wiley.com/doi/10.1111/maps.13533 by CochraneItalia, Wiley Online Library on [27/02/2025]. See the Terms and Conditions (https://onlinelibrary.wiley.com/terms-and-conditions) on Wiley Online Library for rules of use; OA articles are governed by the applicable Creative Commons License

composed of anhydrous silicates, FeNi metal, silicate glass, and sulfides. They have sizes between ~30 μm and >1000 μm (Weisberg et al. 2006; Jones 2012) and typically appear as rounded subspherical droplets, although in some bodies, they have experienced deformation by later parent body processing (e.g., shock flattening due to impact events [Nakamura et al. 1995]). Also common are CAIs—Ca-, Al-rich inclusions, which have refractory compositions, irregular shapes, and either condensation or igneous histories, recorded in their textures. They typically have compositional zoning (Beckett et al. 2006; Weisberg et al. 2006). Alternatively, some inclusions in meteorites are lithic fragments—which are coherent petrographic units embedded within their host rock, but which have distinct properties different from their host. These lithic fragments, also referred to as clasts, are commonly associated with brecciated samples and/or regolith materials, as in the case of Sutters Mill, Kaidun, Lonewolf Nunataks 94101, and many other primitive carbonaceous chondrites (Zolensky et al. 1996, 2014; Lindgren et al. 2013).

Several of the inclusions found within the studied population are most likely chondrule material. Previously Genge et al. (2005) and later Van Ginneken et al. (2012) demonstrated that chondrules either whole or fragmented are relatively common components within MMs and indeed many coarse-grained MMs are exclusive samples of chondrule material (e.g., Genge 2006, 2008). Inclusions in the particles TAM 50.11 and TAM 50.15 (example of potential chondrules are visible on Fig. 8) are best interpreted as chondrules (sizes given in Table 1). Moreover, three particles studied here, TAM 50.09, TAM 50.22, and TAM 50.29, are whole chondrules (Fig. 8). They have coarse-grained textures with rounded margins and resolvable individual (silicate) crystals, FeNi metal droplets, or glassy regions within the inclusion cores.

More recently, Suttle et al. (2019a) described the presence of pseudomorphic chondrules in giant fine-grained MMs. Pseudomorphic chondrules are components of fine-grained matrix resulting from the replacement of former chondrules by phyllosilicate during advanced (parent body) aqueous alteration (Rubin et al. 2007; Weisberg and Huber 2007). Their identification is more challenging (than identifying unaltered chondrules) because the chondrule's primary mineralogy has since been replaced, blurring their contacts with the host and removing several other important diagnostic criteria. Pseudomorphic chondrule identification therefore relies primarily on the observation of relic textures and trace geochemical variations (seen as differing Z-contrast in BSE and CT images)—these features are often subtle, and thus, the designation of features as pseudomorphic chondrules carries a higher degree of uncertainty. Particles TAM 50.25, TAM 50.26, TAM 50.30 (Fig. 8), and TAM 55.01 (all shown in Fig. 8) most likely contain pseudomorphic chondrules, evidenced by small (<250 μm) subspherical regions of fine-grained matrix with differing Z-contrast and/or pore texture. In TAM 50.26 (Fig. 8), an oval-shaped region of matrix can be seen whose pore space has distinctly crescent-shaped voids. These pores, therefore, define a rounded region which appears distinct from the rest of the MM's matrix. However, the best example of a pseudomorphic chondrule is found in TAM 50.30 (Fig. 8) where a nearly perfect circular region of matrix with a distinctly higher porosity can be seen.

In MMs which preserve chondrules (or their pseudomorphs), it is possible to estimate their petrologic grade (in the scheme of Van Schmus and Wood 1967). However, here we are limited to using only the textural criteria available from our tomographic data (see table 3 of Weisberg et al. 2006). Where chondrules have clear and sharp external boundaries, internal geochemical variation, and no evidence of replacement by secondary phases, they are classified as type 3 (i.e., minimally affected by parent body alteration). Conversely, chondrules affected by aqueous alteration are classified as either type 2 or type 1 dependent on the degree of replacement, with completely replaced pseudomorphic varieties present only among the type 1 extensively aqueously altered bodies. Meanwhile, parent bodies subject to thermal metamorphism are classified with higher petrologic grades (4–7). In petrologic grades, above 3 chondrule boundaries are transitional and thus poorly defined against the host's metamorphic groundmass (Weisberg et al. 2006). Based on these simplified textural criteria, we classify the four chondrule-bearing MMs (TAM 50.09, TAM 50.15, TAM 50.11, and TAM 50.22) in the range 2–4, as their chondrules remain discernible and have not been heavily affected by aqueous alteration. In contrast, the four pseudomorphic bearing samples (TAM 50.25, TAM 50.26, TAM 50.30, and TAM 55.01) are either petrologic grade 1 or 2.

Finally, in TAM 50.04 (Figs. 6b and 8), we noted the presence of an equant irregular-shaped dark inclusion. This feature is likely to be a hydrated clast, perhaps a fragment of CI-like or C1 intensely altered material, or a carbonate-rich clast that is held within the matrix of an otherwise less-altered CM/CR-like (or C2) fine-grained matrix. A variety of hydrated clasts with different petrographic characteristics held within CM2 meteorites were previously described by Lindgren et al. (2013) and are likewise reported within MMs (see fig. 10 in Suttle et al. 2017b). Their presence could be regions that accreted higher concentrations of water ice

19455100, 2020, 7, Downloaded from https://onlinelibrary.wiley.com/doi/10.1111/maps.13533 by CochraneItalia, Wiley Online Library on [27/02/2025]. See the Terms and Conditions (https://onlinelibrary.wiley.com/terms-and-conditions) on Wiley Online Library for rules of use; OA articles are governed by the applicable Creative Commons License

and thus produced localized regions with more intense alteration. Alternatively, they may reflect aqueous alteration on a large body followed by catastrophic breakup and re-accretion, as suggested by Lindgren et al. (2013).

The use of μCT has therefore enabled the identification of chondrules, chondrule pseudomorphs, and hydrated clasts within the study population. Identification of substructures can also give indications about the parent body's processing. We have detected intact chondrules in five samples of our data set and the presence of pseudomorphic chondrules inside three of the samples, indicate a strong aqueous alteration. Eight of our 22 samples contain chondrules, this high percentage of samples with chondrules is very noteworthy, confirming the fact that chondrules are relatively common in gian MMs (Genge et al. 2005; Van Ginneken et al. 2012). This high statistic is connected to the size of the samples studied and showed well the interest to focus on giants MMs. Suttle et al. (2019a) argued that MMs are mainly fine-grained intensively altered chondrite (their coarse-grained refractory material has been lost). As with the analysis of any MMs, even giant samples, there are problems associated with how representative an individual MM is of its parent body, as explored previously in Genge et al. (2008), Folco and Cordier (2015), and Suttle et al. (2019a). However, estimations of parent body alteration remain useful because they provide constraints on the approximate degrees and styles of alteration represented among the MM flux. Furthermore, studies such as the present one lend support to the notion that MMs and the larger meteorite population are sampling largely the same source materials, although in different proportions according to size (e.g., Suavet et al. 2010; Cordier and Folco 2014). Here, we detected pseudomorphic chondrules in four MMs among a total of 22, suggesting that >18% of the MM flux at large size fractions (between 400 and 1000 μm) are derived from intensely aqueously altered carbonaceous chondrite asteroids.

First Step of a Characterization Protocol

For rare samples, it is critical to be able to optimize their characterization. As suggested by Uesegi et al. (2013), X-CT will be an important source of information for the analysis of valuable samples collected by future sample return missions. X-CT causes no major damage on the mineral components, but some studies have suggested that X-CT can compromise the natural radiation records of the samples (see e.g., Sears et al. 2016; Hanna and Ketcham 2018). Friedrich et al. (2019) have noticed no variation of the organic component after X-CT irradiation. For the majority of rare samples, it will be critical to analyze the internal distribution of the different components (including the organics) by means of combined tomography (see Dionnet et al. [2018b] for a combination of X-CT and IR-CT) before planning more destructive analyses. We used this initial X-ray 3-D characterization to classify the samples; to collect information about their geological history; and also to identify substructures of interest, such as chondrules. This work is a first step of an efficient analytical sequence optimized for the analysis of valuable extra-terrestrial dust particles with sizes between 100 μm and 1 mm. X-ray 3-D analysis allows us to tailor the most effective analytical technique for each sample for subsequent analysis. For the samples with structures, for instance with well-preserved inclusions, like TAM 50.04, sectioning and polishing of the sample after having embedded it with resin could be envisaged. Then, 2-D techniques could be performed, for example, FTIR spectroscopy (Dionnet et al. 2018a), and FESEM-EDX could be envisaged to give further precise information on their chemical composition. More destructive analyses like oxygen isotopic measurement could be performed to identify the parent bodies of the sample and then to be able to connect morphological properties to classes of asteroids/meteorites. Among our data set, 12 samples have been selected for future O-isotopic research while the remaining samples will be embedded and sectioned to perform more quantitative 2-D analyses.

CONCLUSIONS

We characterized different properties of 22 giant TAM MMs. Porosity, detection of rims, and the position of metallic beads have been used to distinguish scoriaceous MMs and unmelted MMs. We concluded that the porosity of the unmelted samples varies between 0 and 25 vol% while for scoriaceous MMs, it varies between 10 and 40 vol%.

The TAM MMs analyzed here primarily record the early stages of atmospheric entry heating at subsolidus (unmelted MMs) and subliquidus temperatures (scoriaceous MMs). Their porosity increases (above a loosely constrained unheated parent body value), therefore, trace the internal heating of the sample; beyond this basic observation, we demonstrated that internal variations in porosity allow reconstruction of a sample's atmospheric flight history. We identified spinning entry histories for four MMs, among the unmelted particles. Before this study, spinning entry had been observed only in cosmic spherules, but here we show that immature dust is capable of surviving entry without significant melting and that these particles can be analyzed using X-CT. Moreover, we presented the

19455100, 2020, 7, Downloaded from https://onlinelibrary.wiley.com/doi/10.1111/maps.13533 by CochraneItalia, Wiley Online Library on [27/02/2025]. See the Terms and Conditions (https://onlinelibrary.wiley.com/terms-and-conditions) on Wiley Online Library for rules of use; OA articles are governed by the applicable Creative Commons License

first use of X-CT to resolve thermal gradients in MMs using porosity as a metric for peak temperatures in a giant MM that also experienced in-flight fragmentation.

Among unmelted MMs, we proposed different criteria to quantify the strength of the secondary processes undergone on their parent's bodies. A 3-D statistical analysis of pore space in unmelted MMs was performed, suggesting shock fabrics are either absent or weakly developed, similar to the low-grade petrofabrics previously reported among CM chondrites and fine-grained hydrated MMs (Suttle et al. 2017a). We improved the characterization of the degree of aqueous alteration among the MMs flux: we found approximately equal abundances of C1 intensely altered, and C2 moderately altered material, in total contributions from hydrated chondrites could represent as much as 50% of the MMs flux at these size fractions (>400 μm).

Critically, X-CT enabled the nondestructive textural classification of MMs, the identification of subregions of interest as chondrules, pseudomorphic chondrules, and hydrated clasts. Using X-CT 3-D visualizations of internal porosity variation has allowed us to infer the atmospheric entry history of some particles, revealing features such as fragmentation, internal linear thermal gradients, and high spin rates leading to density-dependent phase separation. X-CT will be a very useful tool for the 3-D pre-characterization of rare extraterrestrial samples to be applied prior to subsequent destructive analyses that can be directed toward specific regions of interest, maximizing the data recovered from each particle.

Acknowledgments—MM research at Pisa University and at Napoli "Parthenope" University is supported by MIUR: PNRA16-00029 and PRIN2015-20158W4JZ7. Zelia Dionnet was also supported by the Italian Space Agency within the ASI-INAF agreements I/032/05/0 and I/024/12/0. Martin Suttle was also supported by STFC (Science and Technology Facilities Council) on grant no. ST/R000727/1. We acknowledge SOLEIL for provision of synchrotron radiation facilities. We thank the astrochimie team of IAS (especially Rosario Brunetto, Zahia Djouadi, and Alice Aléon-Toppani) for fruitful discussion and advice during the measurement session. We thank M. Genge and G. Flynn for their constructive comments on the manuscript during review.

Editorial Handling—Dr. Donald Brownlee

REFERENCES

Alexander C.M.O'D., Boss A. P., Keller L. P., Nuth J. A., and Weinberger A. 2007. Astronomical and meteoritic evidence for the nature of interstellar dust and its processing in protoplanetary disks. In *Protostars and planets V*, edited by Reipurth B., Jewitt D., and Keil K. Tucson, Arizona: The University of Arizona Press. pp. 801–813.

Baecker B., Ott U., Cordier C., Folco L., Trieloff M., van Ginneken M., and Rochette P. 2018. Noble gases in micrometeorites from the Transantarctic Mountains. *Geochimica et Cosmochimica Acta* 242:266–297.

Beckett J. R., Connolly H. C., and Ebel D. S. 2006. Chemical processes in igneous calcium-aluminum-rich inclusions: A mostly CMAS view of melting and crystallization. In *Meteorites and the early solar system II*, edited by Lauretta D. S. and McSween H. Y. Tucson, Arizona: The University of Arizona Press. pp. 399–430.

Benedix G. K., Ketcham R. A., Wilson L., McCoy T. J., Bogard D. D, Garrison D. H., Herzog G. F., Xue S., Klein J., and Middleton R. 2008. The formation and chronology of the PAT 91501 impact-melt L chondrite with vesicle–metal–sulfide assemblages. *Geochimica et Cosmochimica Acta* 72:2417–2428.

Blum J., Gundlach B., Krause M., Fulle M., Johansen A., Agarwal J., von Borstel I., Shi X., Hu X., Bentley M. S., Capaccioni F., Colangeli L., Della Corte V., Fougere N., Green S. F., Ivanovski S., Mannel T., Merouane S., Migliorini A., Rotundi A., Schmied R., and Snodgrass C. 2017. Evidence for the formation of comet 67P/Churyumov-Gerasimenko through gravitational collapse of a bound clump of pebbles. *Monthly Notices of the Royal Astronomical Society* 469:S755–S773.

Bowden K. E. 2002. Effects of loading path on the shock metamorphism of porous quartz: An experimental study. PhD thesis, University of London, London, UK.

Campagnola S., Yam C. H., Tsuda Y., Ogawa N., and Kawakatsu Y. 2018. Mission analysis for the Martian Moons Explorer (MMX) mission. *Acta Astronautica* 146:409–417.

Che C. and Glotch T. D. 2012. The effect of high temperatures on the mid-to-far-infrared emission and near-infrared reflectance spectra of phyllosilicates and natural zeolites: Implications for Martian exploration. *Icarus* 218:585–601.

Cordier C., Folco L. 2014. Oxygen isotopes in cosmic spherules and the composition of the near Earth interplanetary dust complex. *Geochimica et Cosmochimica Acta* 146:18–26.

Consolmagno G. J., Britt D. T., and Macke R. J. 2008. The significance of meteorite density and porosity. *Chemie der Erde* 68:1–29.

Cordier C., Baecker B., Ott U., Folco L., and Trieloff M. 2018. A new type of oxidized and pre-irradiated micrometeorite. *Geochimica et Cosmochimica Acta* 233:135–158.

Court R. W. and Tan J. 2016. Insights into secondary reactions occurring during atmospheric ablation of micrometeoroids. *Meteoritics & Planetary Science* 51:1163–1183.

DeCarli P. S., Bowden E., and Seaman L. 2001. Shock-induced compaction and porosity in meteorites (anbstract). *Meteoritics & Planetary Science* 36:A47.

Dionnet Z., Aleon-Toppani A., Baklouti D., Borondics F., Brisset F., Djouadi Z., Sandt C., and Brunetto R. 2018a. Organic and mineralogic heterogeneity of the Paris meteorite followed by FTIR hyperspectral imaging. *Meteoritics & Planetary Science* 53:2608–2623.

19455100, 2020, 7, Downloaded from https://onlinelibrary.wiley.com/doi/10.1111/maps.13533 by CochraneItalia, Wiley Online Library on [27/02/2025]. See the Terms and Conditions (https://onlinelibrary.wiley.com/terms-and-conditions) on Wiley Online Library for rules of use; OA articles are governed by the applicable Creative Commons License

Dionnet Z., Aléon-Toppani A., Borondics F., Brunetto R., Buellet Ac, Djouadi Z., King A., Rubino S., and Troadec D. 2018b. FTIR micro-tomography of five Itokawa particles and one primitive carbonaceous chondrite. *Microscopy and Microanalysis* 24:2100–2101.

Ebel D. S. and Rivers M. L. 2007. Meteorite 3-D synchrotron microtomography: Methods and applications. *Meteoritics & Planetary Science* 42:1627–1646.

Flynn G. F., Consolmagno G. J., Brown P., and Macke R. J. 2018. Physical properties of the stone meteorites: Implications for the properties of their parent bodies. *Chemie der Erde* 78:269–298.

Folco L. and Cordier C. 2015. Micrometeorites. In *EMU notes in mineralogy 15: Planetary mineralogy*, edited by Lee M. R., and Leroux H. Twickenham, UK: European Mineralogical Union. pp. 253–297.

Folco L. Rochette P., Perchiazzi N., D'Orazio M., Laurenzi M. A., and Tiepolo M. 2008. Microtektites from Victoria land transantarctic mountains. *Geology* 36:291–294.

Friedrich J. M. 2008. Quantitative methods for three-dimensional comparison and petrographic description of chondrites. *Computers & Geosciences* 34:1926–1935.

Friedrich J. M. and Rivers M. L. 2013. Three-dimensional imaging of ordinary chondrite microporosity at 2.6 μm resolution. *Geochimica et Cosmochimica Acta* 116:63–70.

Friedrich J. M., Ruzicka A., Macke R. J., Thostenson J. O., Rudolph R. A., Rivers M. L., and Ebel D. S. 2017. Relationships among physical properties as indicators of high temperature deformation or post-shock thermal annealing in ordinary chondrites. *Geochimica et Cosmochimica Acta* 203:157–174.

Friedrich J. M., Macke R. J., Wignarajah D. P., Rivers M. L., Britt D. T., and Ebel D. S. 2008. Pore size distribution in an uncompacted equilibrated ordinary chondrite. *Planetary and Space Science* 56:895–900.

Friedrich J. M. MCLain H.L., Dworkin J.P., Glavin D.P., Towbin W.H., Hill M. and Ebel D.S. 2019. Effect of polychromatic X-ray microtomography imaging on the amino acid content of the Murchison CM chondrite. *Meteoritics & Planetary Science* 54:220–228.

Fulle M., Blum J., and Rotundi A. 2019. How comets work. *The Astrophysical Journal Letters* 879:L8.

Genge M. J. 2006. Igneous rims on micrometeorites. *Geochimica et Cosmochimica Acta* 70:2603–2621.

Genge M. J. 2008b. Koronis asteroid dust within Antarctic ice. *Geology* 36:687–690.

Genge M. J. 2017a. An increased abundance of micrometeorites on Earth owing to vesicular parachutes. *Geophysical Research Letters* 44:1679–1686.

Genge M. J. 2017b. Vesicle dynamics during the atmospheric entry heating of cosmic spherules. *Meteoritics & Planetary Science* 52:443–457.

Genge M. J., Grady M. M., and Hutchison R. 1997. The texture and compositions of fine-grained Antartic micrometeorites —Implications for comparisons with meteorites. *MGeochimica et Cosmochimica Acta* 61:5149–5162.

Genge M. J., Gileski A., and Grady M. M. 2005. Chondrules in Antarctic micrometeorites. *Meteoritics & Planetary Science* 40:225–238.

Genge M. J., Engrand C., Gounelle M., and Taylor S. 2008a. The classification of micrometeorites. *Meteoritics & Planetary Science* 43:497–515.

Genge M. J., Suttle M., and Van Ginneken M. 2016. Olivine settling in cosmic spherules during atmospheric deceleration: An indicator of the orbital eccentricity of interplanetary dust. *Geophysical Research Letters* 43:10,646–10,653.

Genge M. J., Suttle M., and Van Ginneken M. 2017. Thermal shock fragmentation of Mg silicates within scoriaceous micrometeorites reveal hydrated asteroidal sources. *Geology* 45:891–894.

Glavin D. P., and Bada J. L. 2001. Survival of amino acids in micrometeorites during atmospheric entry. *Astrobiology* 1:259–269.

Greshake A., Klock W., Arndt P., Maetz M., Flynn G. J., Bajt S., and Bischoff A. 1998. Heating experiments simulating atmospheric entry heating of micrometeorites: Clues to their parent body sources. *Meteoritics & Planetary Science* 33:267–290.

Gürsoy D., De Carlo F., Xiao X., and Jacobsen C. 2014. Tomopy: A framework for the analysis of synchrotron tomographic data. *Journal of Synchrotron Radiation* 21:1188–1193.

Hanna R. D., Ketcham R. A., Zolensky M., and Behr W. M. 2015. Impact-induced brittle deformation, porosity loss, and aqueous alteration in the Murchison CM chondrite. *Geochimica et Cosmochimica Acta* 171:256–282.

Hanna R. D., and Ketcham R. A. 2018. X-ray computed tomography of planetary materials: A primer and review of recent studies. *Chemie der Erde* 77:547–572.

Jones R. H. 2012. Petrographic constraints on the diversity of chondrule reservoirs in the protoplanetary disk. *Meteoritics & Planetary Science* 47:1176–1190.

Ketcham R. A. 2005. Three-dimensional grain fabric measurements using high-resolution X-ray computed tomography. *Journal of Structural Geology* 27:1217–1228.

Ketcham R. A., and Ryan T. 2004. Quantification and visualization of anisotropy in trabecular bone. *Journal of Microscopy* 213:158–171.

Kitazato K., Milliken R. E., Iwata T., Abe M., Ohtake M., Matsuura S., Arai T., Nakauchi Y., Nakamura T., Matsuoka M., Senshu H., Hirata N., Hiroi T., Pilorget C., Brunetto R., Poulet F., Riu L., Bibring J.-P., Takir D., Domingue D. l., Vilas F., Barucci M. A., Perna D., Palomba E., Galiano A., Tsumura K., Osawa T., Komatsu M., Nakato A., Arai T., Takato N., Matsunaga T., Takagi Y., Matsumoto K., Kouyama T., Yokota Y., Tatsumi E., Sakatani N., Yamamoto Y., Okada T., Sugita S., Honda R., Morota T., Kameda S., Sawada H., Honda C., Yamada M., Suzuki H., Yoshioka K., Hayakawa M., Ogawa K., Cho Y., Shirai K., Shimaki Y., Hirata N., Yamaguchi A., Ogawa N., Terui F., Yamaguchi T., Takei Y., Saiki T., Nakazawa S., Tanaka S., Yoshikawa M., Watanabe S., and Tsuda Y. 2019. The surface composition of asteroid 162173 Ryugu from Hayabusa 2 near-infrared spectroscopy. *Science* 364:272–275.

Kohout T., Kallonen A., Suuronen J-P., Rochette P., Hutzler A., Gattacceca J., Badjukov D. D., Skála R., Böhmová V., and Čuda J. 2014. Density, porosity, mineralogy, and internal structure of cosmic dust and alteration of its properties during high-velocity atmospheric entry. *Meteoritics & Planetary Science* 49:1157–1170.

Lauretta D., Bartels A. E., Barucci M. A., Bierhaus E. B., Binzel R. P., Bottke W. F., Campins H., Chesley S. R., Clark B. C., Clark B. E., Cloutis E. A., Connolly H. C., Crombie M. K., Delbó M., Dworkin J. P., Emery J. P., Glavin D. P., Hamilton V. E., Hergenrother C. W., Johnson C. l., Keller L. P., Michel P., Nolan M. C.,

19455100, 2020, 7, Downloaded from https://onlinelibrary.wiley.com/doi/10.1111/maps.13533 by CochraneItalia, Wiley Online Library on [27/02/2025]. See the Terms and Conditions (https://onlinelibrary.wiley.com/terms-and-conditions) on Wiley Online Library for rules of use; OA articles are governed by the applicable Creative Commons License

Sandford S. A., Scheeres D. J., Simon A. A., Sutter B. M., Vokrouhlický D., and Walsh K. J. 2015. The OSIRIS-REx target asteroid (101955) Bennu: Constraints on its physical, geological, and dynamical nature from astronomical observations. *Meteoritics & Planetary Science* 50:834–849.

Lindgren P., Lee M. R., Sofe M. R., and Zolensky M. E. 2013. Clasts in the CM 2 carbonaceous chondrite Lonewolf Nunataks 94101: Evidence for aqueous alteration prior to complex mixing. *Meteoritics & Planetary Science* 48:1074–1090.

Love S. G. and Brownlee D. E. 1991. Heating and thermal transformation of micrometeoroids entering the Earth's atmosphere. *Icarus* 89:26–43.

Matrajt G., Messenger S., Brownlee D., and Joswiak D. 2012. Diverse forms of primordial organic matter identified in interplanetary dust particles. *Meteoritics & Planetary Science* 47:525–549.

Nakamura T., Tomeoka K., Sekine T., and Takeda H. 1995. Impact-induced chondrule flattening in the Allende CV3 carbonaceous chondrite: Shock experiments. *Meteoritics* 30:344–347.

Nakamura T., Noguchi T., Tsuchiyama A., Ushikubo T., Kita N. T., Valley J. W., Zolensky M. E., Kakazu Y., Sakamoto K., Mashio E., Uesugi K., and Nakano T. 2008. Chondrule like objects in short-period comet 81P/Wild 2. *Science* 321:1664–1667.

Nakamura T., Noguchi T., Tanaka M., Zolensky M. E., Kimura M., Tsuchiyama A., Nakato A., Ogami T., Ishida H., Uesugi M., Yada T., Shirai K., Fujimura A., Okazaki R., Sandford S. A., Ishibashi Y., Abe M., Okada T., Ueno M., Mukai T., Yoshikawa M., and Kawaguchi J. 2011. Itokawa dust particles: A direct link between S-type asteroids and ordinary chondrites. *Science* 333:1113.

Nakamura T., Nakato A., Ishida H., Wakita S., Noguchi T., Zolensky M. E., Tanaka M., Kimura M., Tshuchiyama A., Ogami T., Hashimoto T., Konno M., Uesugi M., Yada T., Shirai K., Fujimura A., Okazaki R., Sandford S. A., Ishibashi Y., Abe M., Okada T., Ueno M., and Kawaguchi J. 2014. Mineral chemistry of MUSES-C Regio inferred from analysis of dust particles collected from the first- and second-touchdown sites on asteroid Itokawa. *Meteoritics & Planetary Science* 49:215–227.

Rochette P., Folco L., Suavet C., Van Ginneken M., Gattacceca J., Perchiazzi N., Braucher R., and Harvey R. P. 2008. Micrometeorites from the Transantarctic Mountains. *Proceedings of the National Academy of Sciences* 105:206–211.

Rubin A. E., Trigo-Rodríguez J. M., Huber H., and Wasson J. T. 2007. Progressive aqueous alteration of CM carbonaceous chondrites. *Geochimica et Cosmochimica Acta* 71:2361–2382.

Sasso M. R., Macke R. J., Boesenberg J. S., Britt D. T., Rivers M. L., Ebel D. S., and Friedrich J. M. 2009. Incompletely compacted equilibrated ordinary chondrites. *Meteoritics & Planetary Science* 44:1743–1753.

Scott E. R. and Krot A. N. 2003. Chondrites and their components. *Treatise on Geochemistry* 1:711.

Sears D. W. G., Sears H., Ebel D. S., Wallace S., and Friedrich J. M 2016. X-ray computed tomography imaging: A not-so-nondestructive technique. *Meteoritics & Planetary Science* 51:833–838.

Standford S. C., Engrand C., Rotundi A. 2016. Organic matter in cosmic dust. *Elements* 12:185–189.

Suavet C., Alexandre A., Franchi I. A., Gattacceca J., Sonzogni C., Greenwood R. C., Folco L., and Rochette P. 2010. Identification of the parent bodies of micrometeorites with high-precision oxygen isotope ratios. *Earth and Planetary Science Letters* 293:313.

Suavet C., Rochette P., Kars M., Gattacceca J., Folco L., and Harvey R. P. 2009. Statistical properties of the Transantarctic Mountains (TAM) micrometeorite collection. *Polar Science* 3:100–109.

Suavet C., Gattacceca J., Rochette P., and Folco L. 2011. Constraining the terrestrial age of micrometeorites using their record of the Earth's magnetic field polarity. *Geology* 39:123–126.

Sugita S., Honda R., Morota T., Kameda S., Sawada H., Tatsumi E., Yamada M., Honda C., Yokota Y., Kouyama T., Sakatani N., Ogawa K., Suzuki H., Okada T., Namiki N., Tanaka S., Iijima Y., Yoshioka K., Hayakawa M., Cho Y., Matsuoka M., Hirata N., Hirata N., Miyamoto H., Domingue D., Hirabayashi M., Nakamura T., Hiroi T., Michikami T., Michel P., Ballouz R.-L., Barnouin O. S., Ernst C. M., Schröder S. E., Kikuchi H., Hemmi R., Komatsu G., Fukuhara T., Taguchi M., Arai T., Senshu H., Demura H., Ogawa Y., Shimaki Y., Sekiguchi T., Müller T. G., Hagermann A., Mizuno T., Noda H., Matsumoto K., Yamada R., Ishihara Y., Ikeda H., Araki H., Yamamoto K., Abe S., Yoshida F., Higuchi A., Sasaki S., Oshigami S., Tsuruta S., Asari K., Tazawa S., Shizugami M., Kimura J., Otsubo T., Yabuta H., Hasegawa S., Ishiguro M., Tachibana S., Palmer E., Gaskell R., Le Corre L., Jaumann R., Otto K., Schmitz N., Abell P. A., Barucci M. A., Zolensky M. E., Vilas F., Thuillet F., Sugimoto C., Takaki N., Suzuki Y., Kamiyoshihara H., Okada M., Nagata K., Fujimoto M., Yoshikawa M., Yamamoto Y., Shirai K., Noguchi R., Ogawa N., Terui F., Kikuchi S., Yamaguchi T., Oki Y., Takao Y., Takeuchi H., Ono G., Mimasu Y., Yoshikawa K., Takahashi T., Takei Y., Fujii A., Hirose C., Nakazawa S., Hosoda S., Mori O., Shimada T., Soldini S., Iwata T., Abe M., Yano H., Tsukizaki R., Ozaki M., Nishiyama K., Saiki T., Watanabe S., and Tsuda Y. 2019. The geomorphology, color, and thermal properties of Ryugu: Implications 695 for parent-body processes. *Science* 364:230.

Suttle M. D. and Folco L. 2020. The extraterrestrial dust flux: size distribution and mass contribution estimates inferred from the Transantarctic Mountain (TAM) micrometeorite collection. *Journal of Geophysical Research: Planets*. 125: e2019JE006241.

Suttle M. D., Genge M. J., and Russell S. S. 2017a. Shock fabrics in fine-grained micrometeorites. *Meteoritics & Planetary Science* 52:2258–2274.

Suttle M. D., Genge M. J., Folco L., and Russell S. S. 2017b. The thermal decomposition of fine-grained micrometeorites, observations from mid-IR spectroscopy. *Geochimica et Cosmochimica Acta* 206:112–136.

Suttle M. D., Folco L., Genge M. J., Russell S. S., Najorka J., and van Ginneken M. 2019a. Intense aqueous alteration on C-type asteroids: Perspectives from giant fine-grained micrometeorites. *Geochimica et Cosmochimica Acta* 245:352.

Suttle M. D., Genge M. J., Folco L., Van Ginneken M., Lin Q., Russell S. S., and Najorka J. 2019b. The atmospheric entry of fine-grained micrometeorites: The role of volatile gases in heating and fragmentation. *Meteoritics & Planetary Science* 54:503–520.

19455100, 2020, 7, Downloaded from https://onlinelibrary.wiley.com/doi/10.1111/maps.13533 by CochraneItalia, Wiley Online Library on [27/02/2025]. See the Terms and Conditions (https://onlinelibrary.wiley.com/terms-and-conditions) on Wiley Online Library for rules of use; OA articles are governed by the applicable Creative Commons License

Taylor S., Matrajt G., Lever J. H., Joswiak D. J., and Brownlee D. E. 2007. Size distribution of Antarctic micrometeorites. *Dust in Planetary Systems* 643:145–148.

Taylor S., Jones K. W., Herzog G. F., Claire H. E. 2011. Tomography: A window on the role of sulfur in the structure of micrometeorites. *Meteoritics & Planetary Science* 46:1498–1509.

Taylor S., Matrajt G., and Guan Y. 2012. Fine-grained precursors dominate the micrometeorite flux. *Meteoritics & Planetary Science* 47:550–564.

Toppani A., Libourel G., Engrand C., and Maurette M. 2001. Experimental simulation of atmospheric entry of micrometeorites. *Meteoritics & Planetary Science* 36:1377–1396.

Tsuchiyama A., Nakamura T., Okazaki T., Uesugi K., Nakano T., Sakamoto K., Akaki T., Iida Y., Kadono T., Jogo K., and Suzuki Y. 2009. Three dimensional structures and elemental distributions of Stardust impact tracks using synchrotron microtomography and X-ray fluorescence analysis. *Meteoritics & Planetary Science* 44:1203–1224.

Tsuchiyama A., Uesugi M., Matsushima T., Michikami T., Kadono T., Nakamura T., Uesugi K., Nakano T., Sandford S. A., Noguchi R., Matsumoto T., Matsuno J., Nagano T., Imai Y., Takeuchi A., Suzuki Y., Ogami T., Katagiri J., Ebihara M., Ireland T. R., Kitajima F., Nagao K., Naraoka H., Noguchi T., Okazaki R., Yurimoto H., Zolensky M. E., Mukai T., Abe M., Yada T., Fujimura A., Yoshikawa M., and Kawaguchi J. 2011. Three-dimensional structure of Hayabusa samples: Origin and evolution of Itokawa Regolith. *Science* 333:1125.

Uesugi M., Uesugi K., Takeuchi A., Suzuki Y., Hoshino M., and Tsuchiyama A. 2013. Three-dimensional observation of carbonaceous chondrites by synchrotron radiation X-ray CT—Quantitative analysis and developments for the future sample return missions. *Geochimica et Cosmochimica Acta* 116:17–32.

Van Ginneken M., Folco L., Cordier C., and Rochette P. 2012. Chondritic micrometeorites from the Transantarctic Mountains. *Meteoritics & Planetary Science* 47:228–247.

Van Ginneken M., Genge M. J., Folco L., and Harvey R. P. 2016. The weathering of micrometeorites from the Transantarctic Mountains. *Geochimica et Cosmochimica Acta* 179:1–31.

Van Schmus W. R. and Wood J. A. 1967. A chemical-petrologic classification for the chondritic meteorites. *Geochimica et Cosmochimica Acta* 31:747–765.

Vokrouhlický D., Nesvorný D., and Bottke W. F. 2008. Evolution of dust trails into bands. *The Astrophysical Journal* 672:696–712.

Watanabe S., Hirabayashi M., Hirata N., Hirata N., Noguchi R., Shimaki Y., Ikeda H., Tatsumi E., Yoshikawa M., Kikuchi S., Yabuta H., Nakamura T., Tachibana S., Ishihara Y., Morota T., Kitazato K., Sakatani N., Matsumoto K., Wada K., Senshu H., Honda C., Michikami T., Takeuchi H., Kouyama T., Honda R., Kameda S., Fuse T., Miyamoto H., Komatsu G., Sugita S., Okada T., Namiki N., Arakawa M., Ishiguro M., Abe M., Gaskell R., Palmer E., Barnouin O. S., Michel P., French A. S., McMahon J. W., Scheeres D. J., Abell P. A., Yamamoto Y., Tanaka S., Shirai K., Matsuoka M., Yamada M., Yokota Y., Suzuki H., Yoshioka K., Cho Y., Tanaka S., Nishikawa N., Sugiyama T., Kikuchi H., Hemmi R., Yamaguchi T., Ogawa N., Ono G., Mimasu Y., Yoshikawa K., Takahashi T., Takei Y., Fujii A., Hirose C., Iwata T., Hayakawa M., Hosoda S., Mori O., Sawada H., Shimada T., Soldini S., Yano H., Tsukizaki R., Ozaki M., Iijima Y., Ogawa K., Fujimoto M., Ho T-M., Moussi A., Jaumann R., Bibring J.-P., Krause C., Terui F., Saiki T., Nakazawa S., and Tsuda Y. 2019. Hayabusa2 arrives at the carbonaceous asteroid 162173 Ryugu—A spinning top–shaped rubble pile. *Science* 364:268–272.

Weisberg M. K., McCoy T. J., and Krot A. N. 2006. Systematics and evaluation of meteorite classification. In *Meteorites and the early solar system II*, edited by Lauretta D. S. and McSween H. Y. Tucson, Arizona: The University of Arizona Press. pp. 19–52.

Weisberg M. K. and Huber H. 2007. The GRO 95577 CR1 chondrite and hydration of the CR parent body. *Meteoritics & Planetary Science* 42:1495–1503.

Woodcock N. H. and Naylor M. A. 1983. Randomness testing in three-dimensional orientation data. *Journal of Structural Geology* 5:539–548.

Zolensky M. E., Ivanov A. V., Yang S. V., Mittlefehldt D. W., and Ohsumi K. 1996. The Kaidun meteorite: Mineralogy of an unusual CM1 lithology. *Meteoritics & Planetary Science* 31:484–493.

Zolensky M., Mikouchi T., Fries M., Bodnar R., Jenniskens P., Yin Q. Z., Hagiya K., Ohsumi K., Komatsu M., Colbert M., and Hanna R. 2014. Mineralogy and petrography of C asteroid regolith: The Sutter's Mill CM meteorite. *Meteoritics & Planetary Science* 49:1997–2016.

19455100, 2020, 7, Downloaded from https://onlinelibrary.wiley.com/doi/10.1111/maps.13533 by CochraneItalia, Wiley Online Library on [27/02/2025]. See the Terms and Conditions (https://onlinelibrary.wiley.com/terms-and-conditions) on Wiley Online Library for rules of use; OA articles are governed by the applicable Creative Commons License